



Evidence that corticofugal propagation of ALS pathology is not mediated by prion-like mechanism

Jelena Scekcic-Zahirovic, Mathieu Fischer, Geoffrey Stuart-Lopez, Thibaut Burg, Johan Gilet, Sylvie Dirrig-Grosch, Christine Marques, Marie-Christine Birling, Pascal Kessler, Caroline Rouaux

► To cite this version:

Jelena Scekcic-Zahirovic, Mathieu Fischer, Geoffrey Stuart-Lopez, Thibaut Burg, Johan Gilet, et al.. Evidence that corticofugal propagation of ALS pathology is not mediated by prion-like mechanism. Progress in Neurobiology, 2021, 200, pp.101972. 10.1016/j.pneurobio.2020.101972 . hal-04014941

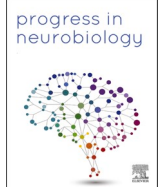
HAL Id: hal-04014941

<https://hal.science/hal-04014941>

Submitted on 4 Mar 2023

HAL is a multi-disciplinary open access archive for the deposit and dissemination of scientific research documents, whether they are published or not. The documents may come from teaching and research institutions in France or abroad, or from public or private research centers.

L'archive ouverte pluridisciplinaire **HAL**, est destinée au dépôt et à la diffusion de documents scientifiques de niveau recherche, publiés ou non, émanant des établissements d'enseignement et de recherche français ou étrangers, des laboratoires publics ou privés.



Evidence that corticofugal propagation of ALS pathology is not mediated by prion-like mechanism

Jelena Scekcic-Zahirovic^{a,1}, Mathieu Fischer^{a,2,5}, Geoffrey Stuart-Lopez^{a,5}, Thibaut Burg^{a,3}, Johan Gilet^a, Sylvie Dirrig-Grosch^a, Christine Marques^{a,4}, Marie-Christine Birling^b, Pascal Kessler^c, Caroline Rouaux^{a,*}

^a Inserm UMR_S 1118, Centre de Recherche en Biomédecine de Strasbourg, Faculté de Médecine, Université de Strasbourg, 67 000, Strasbourg, France

^b Institut Clinique de la souris, 67 400, Illkirch-Graffenstaden, France

^c Inserm UMR_S 38, Centre de Recherche en Biomédecine de Strasbourg, Faculté de Médecine, Université de Strasbourg, 67 085, Strasbourg, France

ARTICLE INFO

Keywords:

Amyotrophic lateral sclerosis
Corticofugal hypothesis
Corticospinal neurons
Cell-autonomous mechanism
Prion-like propagation
SOD1

ABSTRACT

Amyotrophic lateral sclerosis (ALS) arises from the combined degeneration of motor neurons (MN) and corticospinal neurons (CSN). Recent clinical and pathological studies suggest that ALS might start in the motor cortex and spread along the corticofugal axonal projections (including the CSN), either via altered cortical excitability and activity or via prion-like propagation of misfolded proteins. Using mouse genetics, we recently provided the first experimental arguments in favour of the corticofugal hypothesis, but the mechanism of propagation remained an open question. To gain insight into this matter, we tested here the possibility that the toxicity of the corticofugal projection neurons (CFuPN) to their targets could be mediated by their cell autonomous-expression of an ALS causing transgene and possible diffusion of toxic misfolded proteins to their spinal targets. We generated a *Crym-CreER^{T2}* mouse line to ablate the *SOD1^{G37R}* transgene selectively in CFuPN. This was sufficient to fully rescue the CSN and to limit spasticity, but had no effect on the burden of misfolded SOD1 protein in the spinal cord, MN survival, disease onset and progression. The data thus indicate that in ALS corticofugal propagation is likely not mediated by prion-like mechanisms, but could possibly rather rely on cortical hyperexcitability.

1. Introduction

Combined degeneration of corticospinal neurons (CSN) in the motor cortex, and motor neurons (MN) in the brainstem and spinal cord clinically defines amyotrophic lateral sclerosis (ALS), an adult onset neuromuscular disorder that rapidly progresses to full paralysis and death, and the third most frequent neurodegenerative disease after Alzheimer's and Parkinson's diseases (Hardiman et al., 2017). CSN and

MN dual neurodegeneration is central to the understanding of ALS pathophysiology, since diseases affecting only the MN (Kennedy's disease, adult-onset spinal and muscular atrophy) are comparatively less severe (Sorenson, 2012). While ALS mostly occurs sporadically, about 10 % of patients have a familial history of the disease, the most common causative genes being *C9ORF72*, *SOD1*, *FUS* and *TARDBP*, that encodes the TDP-43 protein (Brown and Al-Chalabi, 2017; Chia et al., 2017). The genetics of ALS greatly contributed to the development of cellular and

Abbreviations: CSN, corticospinal neurons; SubCerePN, Subcerebral projection neurons; CFuPN, corticofugal projection neurons; MN, spinal and bulbar motoneurons.

* Corresponding author at: Inserm UMR_S 1118, Centre de Recherche en Biomédecine de Strasbourg, 1 rue Eugène Boeckel, 67000, Strasbourg, France.

E-mail address: caroline.rouaux@inserm.fr (C. Rouaux).

¹ Present address: Neurology department, ZBMF, Systems Neurology Laboratory, Universität Ulm, Ulm, Germany.

² Present address: Department of Paediatrics, John Radcliffe Hospital, University of Oxford, Oxford, UK.

³ Present address: Department of Neurosciences, Experimental Neurology, and Leuven Brain Institute (LBI), KU Leuven-University of Leuven ; VIB, Center for Brain & Disease Research, Laboratory of Neurobiology, 3000 Leuven, Belgium.

⁴ Present address: Department of Neurobiology, Harvard Medical School, Boston, MA 02129, USA; Department of Neurology, Massachusetts General Hospital, Boston, MA 02129, USA.

⁵ Equal contribution.

<https://doi.org/10.1016/j.pneurobio.2020.101972>

Received 28 July 2020; Received in revised form 27 November 2020; Accepted 6 December 2020

Available online 9 December 2020

0301-0082/© 2020 The Authors.

Published by Elsevier Ltd.

This is an open access article under the CC BY-NC-ND license

(<http://creativecommons.org/licenses/by-nc-nd/4.0/>).

animal models of the disease, in particular rodent models (Lutz, 2018) and induced MN from patients' iPSC (Guo et al., 2017). These models in turn allowed dissecting MN degeneration mechanisms, unravelling the combination of cell autonomous and non-cell autonomous contributions (Lee et al., 2016; Ragagnin et al., 2019; Serio and Patani, 2017). Contrastingly, while CSN degeneration has been reported in several animal models of ALS (Brunet et al., 2020), very little is known about the mechanisms that govern their dysfunction and degeneration, and whether combined cell autonomous and non-cell autonomous signalling are involved.

CSN represent a discrete subpopulation of cortical layer V sub-cerebral projection neurons (SubCerePN) which, together with the layer VI corticothalamic neurons, constitute the corticofugal projection neurons (CFuPN), i.e. the main cortical output (Lodato et al., 2014). A growing body of evidence from genetic, pathological and functional studies suggests that ALS may originate in the motor cortex and propagate away from the cerebral cortex along the corticofugal projections (Brunet et al., 2020; Eisen et al., 2017; Geevasinga et al., 2016; Gunes et al., 2020), according to the so-called « corticofugal hypothesis » (Braak et al., 2013). Two schools of thought exist regarding the underlying mechanisms of corticofugal propagation: a prion-like propagation of misfolded proteins (Braak et al., 2013; McAlary et al., 2019; Prasad et al., 2019), and a cortical hyperexcitability leading to aberrant corticofugal neurons excitability and activity and consecutive excitotoxicity to their downstream targets (Eisen et al., 2017; Vucic and Kiernan, 2017). ALS is indeed characterized by aggregates of misfolded protein (TDP-43 mostly, but also SOD1 and FUS) (Brettschneider et al., 2013; Farrawell et al., 2015; Neumann et al., 2006), and early hyperexcitability of the motor cortex that negatively correlates with survival and manifests prior to disease onset (Vucic and Kiernan, 2017).

Because the corticofugal hypothesis of ALS and its putative mechanisms cannot be directly assessed in human, animal models could prove useful. While non-human primate in research is controversial and limited (Abbott, 2014), rodents, and mice in particular could be a good alternative, offering a vast panel of possible genetic manipulations. Major anatomical differences exist between the human and rodent motor systems that need to be taken into consideration. In higher primates, CSN can form both direct, monosynaptic connections onto the MN innervating distal muscles, and indirect polysynaptic connections onto MN innervating proximal muscles (Lemon, 2008; Welniarz et al., 2016). Rodent CSN instead connect exclusively in an indirect polysynaptic manner to MN (Lemon, 2008; Welniarz et al., 2016). However, in spite of these differences, rodents have proven extremely useful in research on rehabilitation upon spinal cord injury or stroke (Caleo, 2015; Loy and Bareyre, 2019), and may therefore prove as useful in studying the cortical contribution to ALS.

In order to experimentally assess the corticofugal hypothesis of ALS, we recently generated a mouse model that ubiquitously expresses a mutant of the murine *Sod1* gene, a condition sufficient to develop ALS-like symptoms and premature death, but that entirely lacks CSN and other SubCerePN (Burg et al., 2020). We demonstrated that absence of this CFuPN population delayed disease onset, reduced weight loss and motor impairment, and increased the survival of *Sod1*^{G86R} mice, suggesting that CFuPN carry detrimental signals to their downstream targets, providing the first experimental evidence of the corticofugal hypothesis of ALS (Burg et al., 2020). What this first study did not address is *i*) the nature of the detrimental message carried along the CFuPN, i.e. prion-like or electrophysiological, and *ii*) whether CSN degeneration relies on combination of cell autonomous and non-cell autonomous mechanisms. To gain insight into these relevant questions, here we took advantage of the *FloxedSOD1*^{G37R} mouse model of ALS that allows genetic ablation of the mutant transgene in selected cells upon Cre-mediated recombination (Boillee et al., 2006), and crossed it to the *CrymCreER*^{T2} mouse line that we purposely designed to genetically target CFuPN. We demonstrate that excision of the mutant *SOD1*^{G37R} transgene from the CFuPN is sufficient to prevent CSN

degeneration and limit spasticity, but does not impact the burden of misfolded SOD1 aggregates in the spinal cord, nor disease onset and progression. The data thus suggest that CSN degeneration mostly relies on cell-intrinsic mechanisms, and that the toxicity of the CFuPN to their downstream targets does likely not rely on the transmission by CFuPN of misfolded proteins to their targets in a prion-like manner.

Initial report of the findings presented here was published as a pre-print on bioRxiv (Scekic-Zahirovic et al., 2020).

2. Materials and methods

2.1. Animals

All animal experiments were performed under the supervision of authorized investigators and approved by the local ethical committee of Strasbourg University (CREMEAS, agreement #00738.01). Animals were housed in the animal facility of the Faculty of Medicine of Strasbourg, with a regular 12 h light/dark cycle, under constant conditions (21 ± 1 °C; 60 % humidity). Standard laboratory food and water were accessible ad libitum throughout all experiments. Knock-in *Crym-CreER*^{T2} mice were generated by the Institut Clinique de la Souris (ICS, Illkirch, France) by homologous recombination. The *Crym* locus was engineered to include a *T2A-CreER*^{T2} cassette downstream of the *Crym* coding sequence. Mice were genotyped by PCR of genomic DNA from tail biopsies using the three following primers: GGTTCTTGCGAACCTCATCACTCGT; CCAGGGATGGCAGTGAAGACC; GCTATCCAACCACAAACA-TGAATAGGG. TdTomato reporter mice (B6.Cg-Gt(Rosa)26Sortm14(CAG-tdTomato)Hze/J) were obtained from The Jackson Laboratory, and *FloxedSOD1*^{G37R} were kindly provided by Dr Don W. Cleveland (Boillee et al., 2006). *Crym-CreER*^{T2} males were crossed with TdTomato females to generate *Crym-CreER*^{T2}/TdTomato to verify Cre-mediated recombination of the reporter gene. *Crym-CreER*^{T2} males were crossed with *FloxedSOD1*^{G37R} females and the F1 generation provided four genotypes of interest: WT/WT; *Crym-CreER*^{T2}/WT; WT/*SOD1*^{G37R}; *Crym-CreER*^{T2}/*SOD1*^{G37R}. At post-natal day 15, all animals received a single i.p. injection of 4-Hydroxytamoxifen (H6278, Sigma) dissolved in corn oil (C8267, Sigma) at the dose of 0.25 mg/g body weight. Males were used for survival and behavioural studies and histology. Mice were followed weekly, and disease progression was rated according to a clinical scale going from score 4 to 0, as previously described (Rouaux et al., 2007). End-stage animals were euthanized upon reaching score 0, i.e. when they were no longer unable to roll over within 10 s after being gently placed on their back (Rouaux et al., 2007). Disease onset was measured as the time of peak of body weight.

2.2. Western blot analyses

For fractionation, immunoblotting sample homogenates (10 % w/v) were prepared in PBS and homogenized with a Potter. Samples were combined at 1:1 with 2% Sarkosyl (N-lauroylsarcosine) in PBS. Benzonase (50 U/mL, Sigma) was added to remove DNA and homogenates were incubated with constant agitation at 37 °C for 30 min, followed by ultracentrifugation at 100 000 g for 40 min at 4 °C. Supernatants were saved as soluble fractions. Pellets were washed in 1% Sarkosyl in PBS and further spun at 100 000 g for 40 min. Supernatants were discarded and pellets solubilized in 4% SDS. Protein quantification was performed using a BCA Assay Reagent Kit (UP95424, Uptima). Samples (10 µg) were boiled in the appropriate volume of Laemmli buffer, resolved by SDS-PAGE (Stain free gel gradient 4–20 %, Biorad) and transferred to a 0.45 µm nitrocellulose membrane (Bio-Rad) using a semi-dry Transblot Turbo transfer system (Bio-Rad). Membranes were probed with a mouse anti-human misfolded SOD1 antibody (1/1000, B8H10, Médimabs), followed by an HRP-conjugated goat anti-mouse antibody (1/5000, BI2413C, Abliance). Protein bands detection by ECL Lumina Forte (Millipore) and quantification were performed on a chemiluminescence detector (Chemidoc, Bio-Rad).

2.3. Semi-quantitative PCR on genomic DNA and gel electrophoresis

Cortical layers were microdissected under a SMZ18 microscope (Nikon) from three adjacent 1 mm-thick coronal brain sections obtained using a stainless steel coronal brain matrix (Harvard Apparatus, MA). Cortical layers and spinal cord were harvested, rapidly frozen in liquid nitrogen and stored at -80 °C until use. Genomic DNA was extracted using the conventional phenol-chloroform/proteinase-K method. 0.5 µg of DNA was amplified using a mix of the following primers:

h *SOD1*: CAGCAGTCACATTGCCAGGTCTCCAACATG; CCAAGATGCTTAACCTCTTGAATCAATGGC

m *Actb*: AGAGGGAAATCGTGCGTGAC; CAATAGTGATGACCTGGCCGT

The PCR products were separated on a 3.0 % agarose gel using 1X TAE buffer containing ethidium bromide and were visualized under UV light, and the gels were photographed using a UV gel documentation system. A DNA molecular weight ladder (Life Technologies) was run on every gel to confirm expected molecular weight of the amplification product. For quantification, band intensities were measured using ImageJ (NIH).

2.4. qPCR analyses

Cortical layers, spinal cord and muscle tibialis anterior were harvested and rapidly frozen in liquid nitrogen and stored at -80 °C until analysis. Total RNA was extracted using TRIzol reagent (Invitrogen) and stainless-steel bead in a Tissue Lyser (Qiagen). 1 µg of RNA was reverse transcribed using the iScript cDNA synthesis kit (Bio-Rad). Quantitative PCR (qPCR) was performed with the IQ SYBR Green Supermix (Bio-Rad). Gene expression was normalized by calculating a normalization factor using *Gusb*, *Actb* and *Hsp90ab1* as reference genes for the nervous tissues, and *H1h2bc*, *H2AC* and *H2AX* as reference genes for the muscular tissues. The following primer were used:

h*SOD1*: CTGTACCAGTGCAGGTCCTC; CCAAGTCTCCAACATGCC TCT

Crym: CACATCAATGCTGTTGGAGCC; TCCACATACAGCACCGCTTG

Gusb: CGAGTATGGAGCAGACGCAA; AGCCTTCTGGTACTCTCACT

Actb: ATGTGGATCAGCAAGCAGGA; AGCTCAGTAACAGTCCGCCT

Hsp90ab1: TACTACTCGGCTTTCCCGTCA; CCTGAAAGGCAAAGGTCTCCA

AChR-γ: GAGAGCCACCTCGAAGACAC; GACCAACCTCATCTCCC TGA

H1h2bc: AACAAGCGCTCGACCATCA; GAATTCGCTACGGAGGCTT ACT

H2AC: CAACGACGAGGAGCTCAACAAG; GAAGTTTCCGCGAGATTCT GTTGC

H2AX: TCCTGCCCAACATCCAGG; TCAGTACTCCTGAGAGGCCTGC

2.5. Motor tests

For all motor tests, mice were trained from 24 to 25 weeks of age, and then followed from 26 weeks of age until death, on a daily basis for general health and neurological symptoms, and once a week for body weight, muscle grip strength, inverted grid test and CatWalk. Each motor session consisted of three trials and the results represent the mean of these three trials. Muscle strength was measured using a strength grip meter (Bioseb, BIO-GS3). Four limbs hang test that allows measuring the ability of mice to use sustained limb tension to oppose gravitational force was used as previously described (Burg et al., 2020; Scekic-Zahirovic et al., 2017). Mouse gait was analysed with the CatWalk XT (Noldus Information Technology) which generates numerous parameters for quantitative and qualitative analysis of individual footprint and gait (Vergouts et al., 2015). Recordings were performed under the conditions previously described (Burg et al., 2020; Scekic-Zahirovic et al., 2017). Each mouse was allowed to cross freely the recording field of the runway with three independent attempts. Criteria for data

collection were i) crossing the field in less than 10 s and ii) a walking speed variation of less than 60 %. The six following gait and coordination parameters were analysed: Run Average Speed, Hind limbs Stand Index, Hind limbs Max Contact Max Intensity Mean, Hind limbs Max Contact Mean Intensity Mean, Hind limbs print area and Hind limbs stride length.

2.6. Electromyography

All recordings were performed with a standard EMG apparatus (Dantec) on mice anesthetized with a solution of Ketamine (Imalgène 1000®, Merial; 90 mg/kg body weight) and Xylazine (Rompun 2%®, Bayer; 16 mg/kg body weight) and kept under a heating mat to maintain physiological body temperature (≈31 °C). Electrical activity was monitored on gastrocnemius and tibialis anterior muscles of both limbs for at least 2 min, as previously described (Rouaux et al., 2007). For each muscle, a score of 0 (innervated, i.e. not presenting any spontaneous muscle activity) or 1 (denervated, i.e. presenting spontaneous muscle activity) was given, and the total scores of the four muscles were summed.

2.7. Tail spasticity

Tail spasticity of end stage mice was determined and quantified as previously described (El Oussini et al., 2017). Briefly, a monopolar needle electrode (Medtronic, 9013R0312, diameter 0.3 mm) was inserted in segmental tail muscles of paralyzed mice to record reflex activity. Muscles spasms were evoked with mechanical stimulation of the tail. For quantification of the response, value of maximal amplitude (in mV) of long lasting reflex signal was measured after stimulation, using ImageJ (NIH).

2.8. In situ hybridization

The cDNA clone for mu *Crystallin* (Crym) is a kind gift from the Arlotta lab. Riboprobes were generated as previously described (Arlotta et al., 2005). Nonradioactive *in situ* hybridization was performed on 40 µm vibratome coronal brain sections 0.14 mm anterior to Bregma. Selected sections were mounted on superfrost slides and processed using reported methods (Lodato et al., 2011). Bright field 10X tile images were acquired with an AxioImager.M2 microscope (Zeiss) equipped a high-resolution B/W camera (Hamamatsu), and run by the ZEN 2 software (Zeiss).

2.9. Retrograde labelling of the CSN

CSN were labelled as previously described (Marques et al., 2019). Briefly, animals were deeply anesthetized with an intraperitoneal injection of Ketamine (Imalgène 1000®, Merial; 120 mg/kg body weight) and Xylazine (Rompun 2%®, Bayer; 16 mg/kg body weight) solution and placed on a heating pad. Laminectomy was performed in the C3-C4 cervical or lumbar (L1-L2) region of the spinal cord, and the dura was punctured using a pulled glass capillary lowered to the dorsal funiculus. Five pressure microinjections of 23 nl of Fluorogold (Fluorochrome) were performed on each side of the dorsal funiculus (Drummond Scientific, Nanoject II). Five days after injection, or upon reaching end-stage, mice were euthanized for histological procedures (see below)

2.10. General histological procedures

Animals were deeply anesthetized with an intraperitoneal injection of Ketamine (Imalgène 1000®, Merial; 120 mg/kg body weight) and Xylazine (Rompun 2%®, Bayer; 16 mg/kg body weight), and transcardially perfused with cold 0.01 M phosphate buffered saline (PBS), followed by cold 4% PFA in 0.01 M PBS. Brains, spinal cords, gastrocnemius and tibialis were post-fixed in the same fixative solution

overnight (nervous tissues) or for 1 h (muscles) and stored in PBS 0.01 M at 4 °C until use. Fixed brains and spinal cords were cut in 40 µm thick sections on a vibratome (Leica Biosystems, S2000).

Immunohistochemistry was performed on brain and spinal cord sections at room temperature. Sections were first immersed in 3% hydrogen peroxide (H₂O₂) to remove endogenous peroxidase activity, and washed with PBS, incubated with 5% horse serum and 0.5 % triton X-100 in PBS for 30 min and incubated with primary antibody overnight. After rinsing in PBS, sections were incubated with biotinylated secondary antibody for 2 h, rinsed in PBS and incubated 1 h with the Vectastain ABC Kit (Vector Laboratories, PK7200). Revelation was performed by incubating the sections in 0.075 % 3,3'-diaminobenzidine tetrahydrochloride (D5905, Sigma) and 0.002 % H₂O₂ in 50 mM Tris HCl.

For immunofluorescence, brain and spinal cord sections were heated at 80 °C in citrate buffer pH6.0 for 30 min and incubated with 5% horse serum and 0.5 % triton X-100 in PBS for 1 h before being incubated with primary antibody overnight at 4 °C. After rinsing in PBS, sections were incubated with Alexa-conjugated secondary antibody for 2 h, rinsed in PBS and water and mounted with DPX mounting solution (Sigma, 06522-100ML).

The primary antibodies used in this study are the following: goat anti-Td-Tomato (MyBiosource, MBS448092, 1/100), rabbit anti-Td-Tomato (Rockland, 600-401-379, 1/100), mouse anti-CRYM (Abnova AA215-314, 1/100), rabbit anti-CRE (BioLegend 908001, 1/100), rat anti-CTIP2 (Abcam ab18465, 1/100), rabbit anti-TLE4 (Santa Cruz sc-9125, 1/100), mouse anti-SATB2 (Abcam ab21502, 1/50) mouse anti-PV (Sigma P3088, 1/1000), goat anti-TPH2 antibody (Abcam ab121013, 1/500), goat anti-choline acetyltransferase (Merk Millipore AB144 P, 1/25), mouse anti-human SOD1 (MediMabs, MM-0070-P, clone B8H10, 1/100), mouse anti-P62 (Abcam ab56416, 1/100), rabbit anti-GFAP (Dako Z0334, 1/100), goat anti-Iba1 (Abcam ab5076, 1/100); biotinylated and Alexa-conjugated secondary antibodies (1/500) were purchased from Jackson.

Images were captured using an AxioImager.M2 microscope (Zeiss) equipped with a structured illumination system (Apotome, Zeiss) and a high-resolution B/W camera (Hamamatsu), and run by the ZEN 2 software (Zeiss). Experimenters blinded to the genotypes performed the neuronal counts and NMJ assessments.

2.11. Brain histological analyses

Brains sections from Fluorogold injected animals were mounted on slides with DPX mounting solution (Sigma, 06522). Fluorogold-positive neurons were manually counted, on both hemispheres, within layer V, from M2 medially to S1 laterally. IBA1 and GFAP intensities were quantified using ImageJ software (NIH, MD, USA). Three regions of interest (ROI) were created and used for all images. The three ROI were placed respectively over the cortical layers II/III and V and over the cingulate cortex for background. Background was subtracted from intensities of the cortical layers II/III and V ROI. For each animal 2 pictures corresponding to each hemisphere were analysed. Serotonergic neurons were quantified from individual coronal sections located at Bregma -4.72 mm.

2.12. Spinal cord histological analyses

Lumbar (L5) spinal motor neurons from two sections separated by 320 µm were mounted on slides, dried at 40 °C on a hot plate for 3 h and stained with 1% toluidine blue solution for 1 min, rinsed with water, dehydrated and mounted. Two images per section (one per ventral horn) were captured and motor neurons (defined as cells with an area larger than 350 µm²) were quantified using ImageJ (NIH). hSOD1, GFAP, IBA1 and P62 intensities were quantified using ImageJ software (NIH). For each image, ROI were manually drawn following the natural border between grey and white matter. Intensities were quantified similarly to

IBA1 and GFAP in the brain (see above).

2.13. Muscle histological analyses

Tibialis anterior muscles were dissected into bundles and processed for immunofluorescence using a combination of rabbit anti-synaptophysin (Eurogentec, 1/50) and rabbit anti-neurofilament antibodies (Eurogentec, 1/50) followed by an Alexa-conjugated donkey anti-rabbit 488 (Jackson, 1/1 000), and rhodamine conjugated α-bungarotoxin (Sigma, T0195), as previously described (Marques et al., 2019). On average 100 NMJ per animals were examined by experimenters blinded to the genotype.

2.14. Statistics

Data are presented as mean ± standard error of the mean (SEM). Statistical analyses were performed using GraphPad Prism 6 (GraphPad, CA). Student's *t*-test was used for comparison between two groups, 1-way or 2-way analysis of the variance, followed by Tukey's multiple comparison post hoc test and 2-way repeated measures (RM) analysis of the variance, followed by Bonferroni's multiple comparison post hoc test were applied for three or more groups. For survival and disease onset analysis, animals were evaluated using log-rank test (Mantel-Cox). Fischer exact test was used to determine significant different proportion. Results were considered significant when *p* < 0.05.

3. Results

3.1. Mutant SOD1^{G37R} protein remains soluble in the cerebral cortex of mice

In *Sod1*^{G86R} mice, absence of corticofugal neurons proved to be beneficial, providing the first experimental evidence of the corticofugal hypothesis of ALS (Burg et al., 2020). To test whether corticofugal propagation relies on axonal transport of soluble misfolded SOD1 protein, and synaptic contact to the spinal cord, as proposed for TDP-43 dissemination in patients (Braak et al., 2013), we investigated the presence and solubility of misfolded SOD1 protein in the cerebral cortex, brain stem and spinal cord of *SOD1*^{G37R} mice. First, we performed immunolabellings on coronal sections from the brain, brainstem and lumbar spinal cord of wild-type and *SOD1*^{G37R} mice at presymptomatic (256 ± 8 days of age), symptomatic (244 ± 6 days of age) and disease end stages (432 ± 45 days of age) to reveal the misfolded human SOD1 protein (Fig. 1A). While the brainstem and spinal cord displayed accumulation of SOD1-positive aggregates overtime, the brain in general and the cerebral cortex in particular remained devoid of aggregates and only a very small number of them could be detected in the cerebral cortex of end-stage animals (Fig. 1A). Similarly, little to no SOD1-positive aggregates were detected in the dorsal funiculus where the corticospinal projections travel (Fig. 1A). To further investigate misfolded human SOD1 protein solubility in the different parts of the central nervous system, we performed protein fractionation experiments and separated soluble and insoluble fractions from the cerebral cortex, brain stem and spinal cord of end-stage *SOD1*^{G37R} mice to reveal misfolded human SOD1 protein by Western blot (Fig. 1B). Band quantification revealed that the cerebral cortex displayed a significantly smaller proportion of insoluble SOD1 protein in comparison with the brain stem and spinal cord (One-way ANOVA followed by multiple comparisons, *p* = 0.0042 and *p* = 0.0244 respectively, Fig. 1C). The data indicate that misfolded human SOD1 protein remains essentially soluble in the cerebral cortex, and suggests that it could be diffused and transmitted along the corticofugal projections.

3.2. Generation of *Crym-CreER*^{T2} mice

To test whether possible transmission of misfolded human SOD1

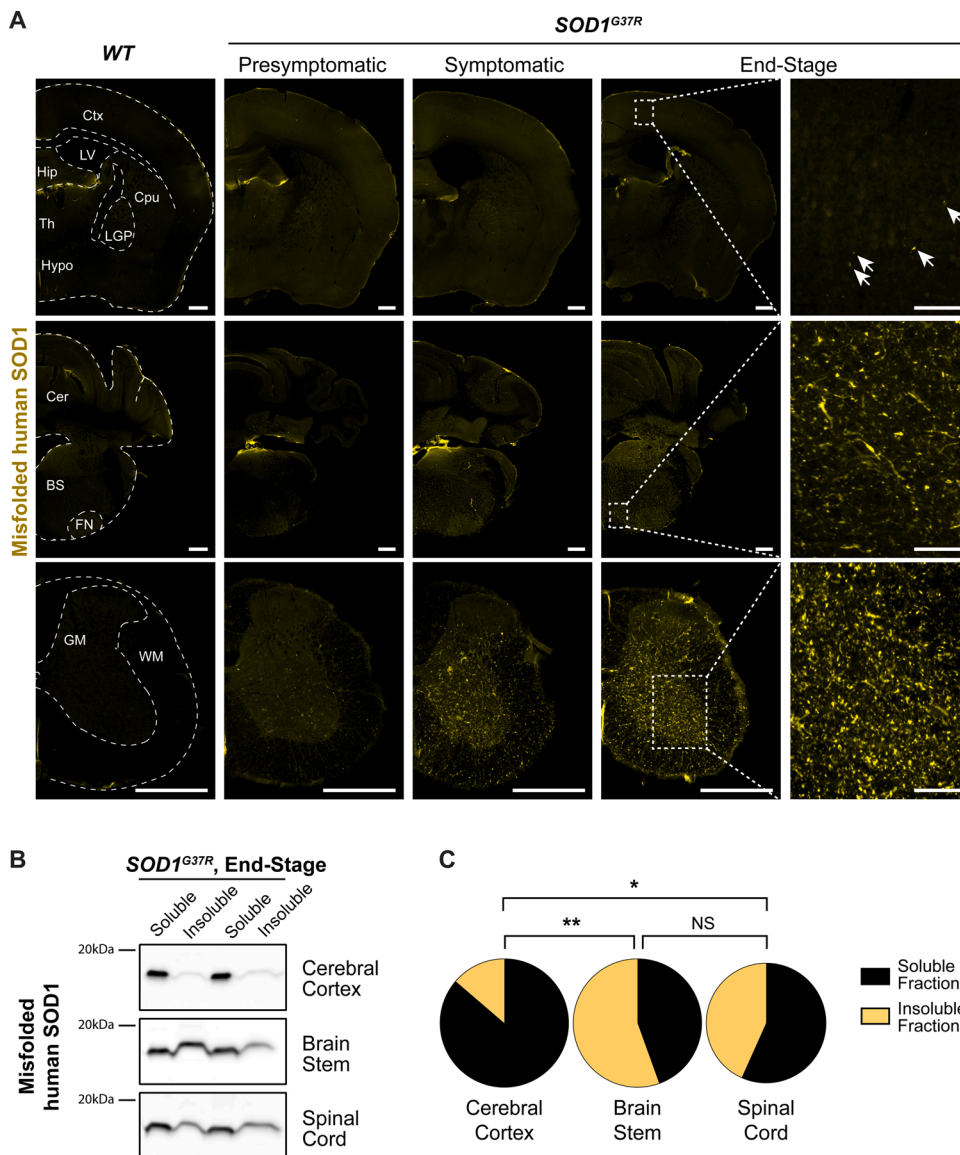


Fig. 1. Mutant SOD1 protein remains soluble in the cerebral cortex.

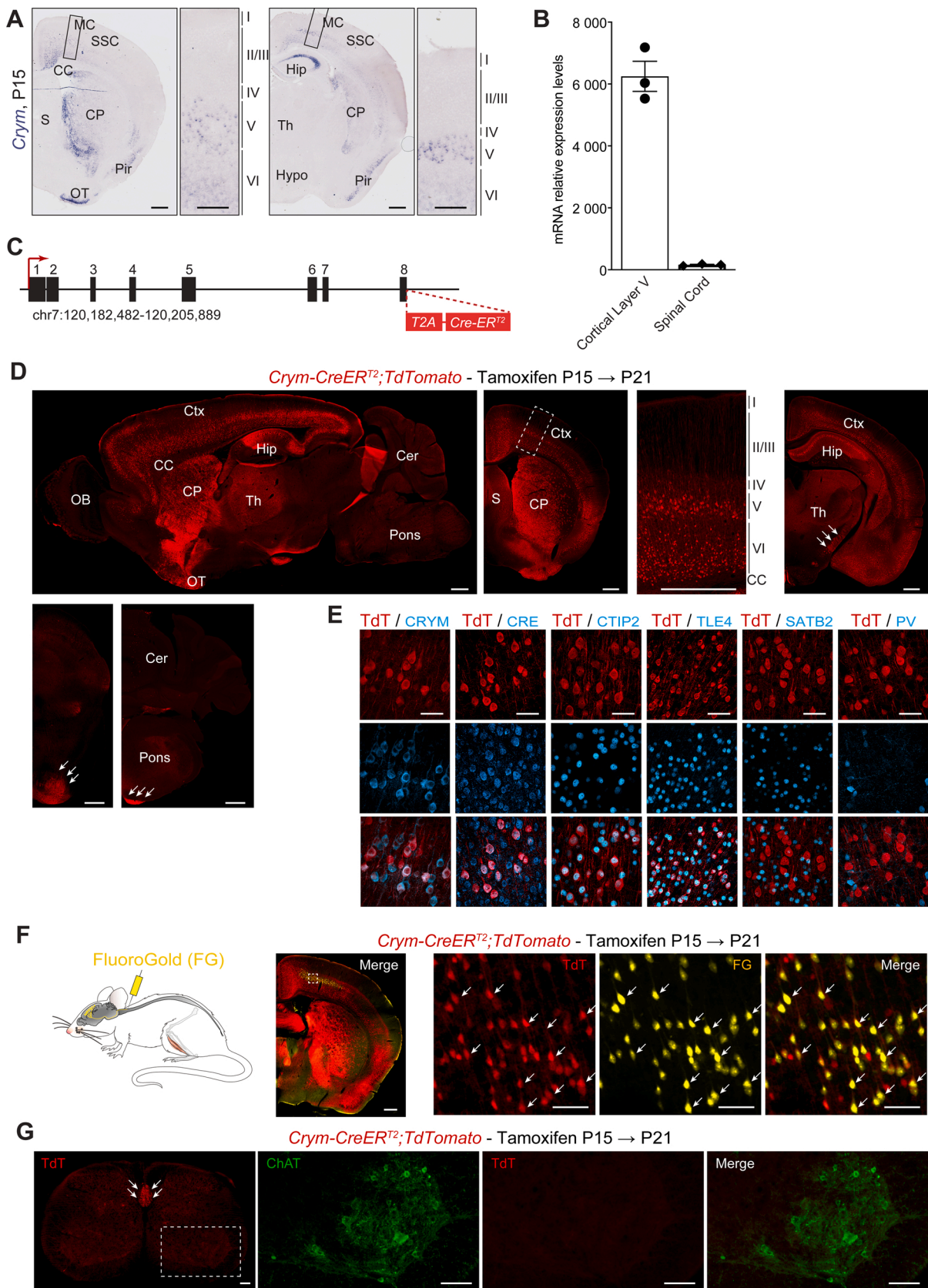
A. Representative images of immunofluorescence on brain and lumbar spinal cord coronal sections from *SOD1^{G37R}* mice harvested at pre-symptomatic, symptomatic and disease end-stage ages, and control wild-type animal (WT), showing time-dependent accumulation of aggregates of the misfolded human SOD1 protein in the brainstem and spinal cord, but not the cerebral cortex, with a few exceptions (arrows). $N = 4$ animals per genotype. Scale bar 500 μm and 100 μm in close-ups. Ctx: cerebral cortex; LV: lateral ventricle; Hip: hippocampus; Th: thalamus; Hypo: hypothalamus; Cpu: caudate putamen; LGP: lateral globus pallidus; Cer: cerebellum; BS: brain stem; FN: facial nucleus; GM: grey matter; WM: white matter.

B. Representative immunoblottings for misfolded human SOD1 protein detected in the soluble and insoluble fractions of homogenates from the cerebral cortex, brain stem and spinal cord of end-stage *SOD1^{G37R}* mice.

C. Pie charts representing the relative proportions of misfolded human SOD1 protein present in the soluble and insoluble fractions of homogenates from the cerebral cortex, brain stem and spinal cord of end-stage *SOD1^{G37R}* mice $N = 4$ animals. One-way ANOVA followed by Tukey's multiple comparisons test. * $p < 0.05$, ** $p < 0.01$.

protein by the corticofugal neurons could contribute to their toxicity onto their downstream targets, we designed experiments to selectively remove misfolded human SOD1 protein from the CFuPN. We generated a mouse line to restrict the expression of the Cre recombinase within the CFuPN populations composed of the layer V SubCerPN that include the discrete population of CSN, and the layer VI corticothalamic neurons. Within the cerebral cortex, expression of *Mu-crystallin* (*Crym*) was found restricted to the CFuPN (Arlotta et al., 2005). We further confirmed this pattern of expression by conducting *in situ* hybridization analyses at postnatal days (P) P1 and P15, and in the adult mouse brain (Fig. 2A, and data not shown). At P15, *Crym* expression was detected in the cingulate cortex, the layer V of the motor and somatosensory cortex, the piriform cortex, the olfactory tubercle, and, at lower level, in the layer VI of the cerebral cortex where corticothalamic neurons are located (Fig. 2A). *Crym* expression was also detected in the most medial part of the caudate putamen, and the CA1 and CA2 regions of the hippocampus (Fig. 2A). To verify that *Crym* was not expressed in the spinal cord, where lower motor neurons (MN) are located, we ran qPCR on mRNA extracted from layer V of the cerebral cortex and the lumbar part of the spinal cord of 4 months old wild-type mice (Fig. 2B). We did not detect *Crym* expression in the spinal cord (Fig. 2B; Unpaired *t*-test;

$p = 0.0002$). We thus designed a knock-in mouse line to restrict the tamoxifen-inducible Cre recombinase (*CreER^{T2}*) within the *Crym* locus, downstream of the coding sequence, and separated from it by a T2A sequence. This allowed to maintain *Crym* endogenous expression and to obtain a spatial and temporal expression of *CreER^{T2}* similar to that of endogenous *Crym* (Fig. 2C). We then crossed the *Crym-CreER^{T2}* line to the TdTomato reporter line (Madisen et al., 2009), administered a single dose of tamoxifen to P15 double transgenic mice, and sacrificed the animals at P21 to verify *Crym-CreER^{T2}*-mediated recombination of the reporter gene (Fig. 2D). Analyses of sagittal and coronal sections revealed robust TdTomato expression throughout the whole cortical layers V and VI and in the upper layers of the frontal cortex (Fig. 2D). Similarly to endogenous *Crym* expression, TdTomato-positive cells were also detected in the caudate putamen and the CA1 and CA2 regions of the hippocampus. Scattered Td-Tomato-positive cells were also found in the olfactory bulb and cerebellum. Importantly, no Td-Tomato positive cells could be detected in the brainstem and spinal cord where MN are located. Finally, Td-Tomato positive axons were detected as tracts within the internal capsule, cerebral peduncle and dorsal funiculus of the spinal cord, in accordance with Td-Tomato expression by SubCerPN and CSN, and as diffused axons in the parenchyma of the thalamus, in



(caption on next page)

Fig. 2. Generation of the knock-in *Crym-CreER^{T2}* mouse line.

A. Representative images of *in situ* hybridization on brain coronal sections from a P15 wild-type mouse showing *Crym* expression. Scale bars 500 μ m and 200 μ m in close-ups.

B. Graph bar representing RT-qPCR results of relative *Crym* expression in the layer V of the cerebral cortex and in the spinal cord.

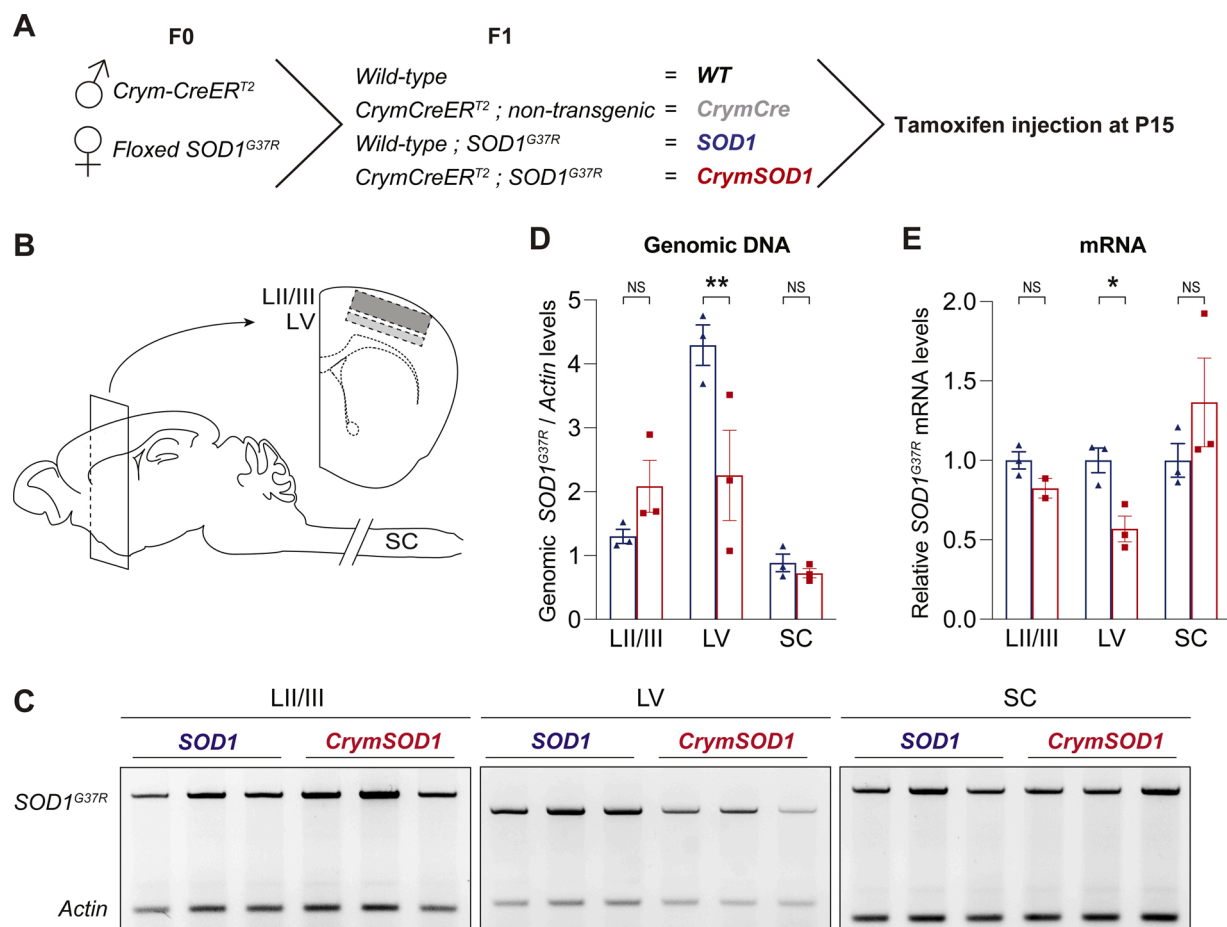
C. Schematic representation of the gene targeting strategy to generate the knock-in and tamoxifen-inducible *Crym-CreER^{T2}* mouse line.

D. Representative immunofluorescence images of sagittal and coronal sections of brains from P21 *Crym-creER^{T2};TdTomato* double transgenic mice upon induced recombination of the reporter by tamoxifen injection at P15. Arrows indicate Td-Tomato-positive corticospinal tract at different rostro-caudal levels. Scale bar 500 μ m.

E. Representative optical sectioning images by structured illumination of immunofluorescence showing the colocalization of cortical layer V Td-Tomato-positive cells together with the CRE recombinase, the layer V subcerebral projection neuron markers *CRYM* and *CTIP2*, and of cortical layer VI Td-Tomato-positive cells together with the layer VI corticothalamic neuron marker *TLE4*. Contrastingly no co-localization with the callosal projection neuron marker *STAB2* or the interneuron marker *PV* could be observed. Scale bar 50 μ m.

F. *Crym-creER^{T2};TdTomato* double transgenic mice received tamoxifen injection at P15 and underwent retrograde labelling of the CSN by injection of FluoroGold into the cervical part of the dorsal funiculus (left schematic). Representative immunofluorescence images of a coronal brain section (right panel) showing Td-Tomato expression and FluoroGold, and their colocalization within the layer V of the motor cortex. Scale bar 500 μ m and 50 μ m in the close-ups.

G. Representative immunofluorescence images of a section of the lumbar spinal cord from P21 *Crym-creER^{T2};TdTomato* double transgenic mice showing Td-Tomato-positive CST in the ventral part of the dorsal funiculus, and absence of Td-Tomato expression in the rest of the spinal cord, and more particularly in the ChAT-positive MN of the ventral horn. Scale bar 100 μ m. MC: motor cortex; SSC: somatosensory cortex; CC: corpus callosum; S: septum; CP: cerebral peduncle; Pir: Piriform cortex; OT: olfactory tubercle; Hip: hippocampus; Th: thalamus; Hypo: hypothalamus; OB: olfactory bulb; Ctx: cortex; Cer: cerebellum.

**Fig. 3.** Selective ablation of *SOD1^{G37R}* transgene in the cortical layer V.

A. Schematic representation of mice cross-breeding to obtain the four genotypes of interest: wild-type (WT); *CrymCreER^{T2};non-transgenic* (*CrymCre*); wild-type; *SOD1^{G37R}* (*SOD1*), and *CrymCreER^{T2};SOD1^{G37R}* (*CrymSOD1*).

B. Schematic representation of the mouse central nervous system indicating the microdissected areas: layers II/III (LII/III) and V (LV) of the cerebral cortex and the lumbar portion of the spinal cord (SC).

C. Representative images of agarose gels of PCR on genomic DNA to detect the levels of genomic *SOD1^{G37R}* transgene LII/III, LV and lumbar spinal cord of *SOD1* (blue) and *CrymSOD1* (red) mice.

D. Bar graph representing the ratio of genomic *SOD1^{G37R}/beta Actin* obtained upon quantification of the bands on the agarose gels (C.) in *SOD1* (blue) and *CrymSOD1* (red) mice. N = 3 animals per genotype. Multiple *t*-test, ***p* < 0.01.

E. Bar graph representing qPCR analyses of the *SOD1^{G37R}* transgene expression levels in *SOD1* (blue) and *CrymSOD1* (red) mice. Multiple *t*-test, **p* < 0.05.

accordance with Td-Tomato expression by layer VI corticothalamic neurons (Fig. 2D). To further verify the identity of Td-Tomato-positive cells present in the cortical layers V and VI, we ran a series of immunolabelling and colocalization analyses using optical sectioning by structured illumination (Fig. 2E). As expected, Td-Tomato expression was restricted to CRYM-expressing neurons and CRE-expressing cells. Td-Tomato also colocalized with CTIP2, a transcription factor expressed at high levels by layer V SubCerePN, and at lower levels by layer VI corticothalamic neurons, and with TLE4 a transcription factor expressed by layer VI corticothalamic neurons (Molyneaux et al., 2007). Importantly, Td-Tomato did not colocalize with SATB2, a transcription factor that selectively labels callosal projection neurons across all cortical layers (Fame et al., 2011; Molyneaux et al., 2007), nor with Parvalbumin-positive (PV) inhibitory GABAergic interneurons (Tremblay et al., 2016) (Fig. 2E). To further test whether the chosen strategy could induce recombination within the disease-relevant CSN, we retrogradely labelled this neuronal population in the *Crym-CreER^{T2}*;Td-Tomato double transgenic mice by injecting Fluorogold (FG) within the cervical portion of the dorsal funiculus. Microscopy analyses in the cortical layer V of the motor cortex revealed colocalization of Td-Tomato with FG (Fig. 2F). Finally, we verified the absence of recombination within the spinal cord. As expected, Td-Tomato positive corticospinal tract (CST) was detected in the ventral part of the dorsal funiculus, but no Td-Tomato positive cell could be detected within the white or the grey matter (Fig. 2G). Importantly, ChAT-positive MN of the ventral horn were devoid of Td-Tomato expression (Fig. 2G). Together, the data indicate that *Crym-CreER^{T2}* expression faithfully recapitulates *Crym* expression and allows the genetic targeting of CFuPN and CSN in particular.

3.3. Genetic ablation of *SOD1^{G37R}* from *Crym-CreER^{T2}* expressing cells

To test the effect of selective removal of an ALS-related transgene from the CSN and other CFuPN, we took advantage of the *Floxed SOD1^{G37R}* transgenic mouse line (Boillee et al., 2006) in which the mutant transgene *SOD1^{G37R}* can be excised upon Cre-mediated recombination, and crossed it to our newly generated *CrymCre-ER^{T2}* line. We obtained 4 genotypes of interest, which we followed over time: *wild-type-non-transgenic* (WT), *CrymCreER^{T2}-non-transgenic* (*CrymCre*), *wild-type-SOD1^{G37R}* (*SOD1*) and *CrymCreER^{T2}-SOD1^{G37R}* (*CrymSOD1*) (Fig. 3A). All animals received a single dose of Tamoxifen at P15 (Fig. 3A), using similar conditions as those that allowed robust recombination of the reporter gene (Fig. 2D-G). To verify *SOD1^{G37R}* transgene excision in the cortical layer V of *CrymSOD1* animals, compared to their *SOD1* littermates, we microdissected the cortical layers II/III and V, along with the spinal cord of four month-old animals (Fig. 3B), extracted genomic DNA and mRNA and ran PCR and RT-qPCR analyses respectively. Combined amplification of the human *SOD1^{G37R}* transgene and the murine *beta Actin* gene from genomic DNA followed by band quantification and ratio calculation of human *SOD1^{G37R}* transgene band intensity on *beta Actin* gene band intensity revealed a significant decrease of human *SOD1^{G37R}* transgene in the cortical layer V, and not in the cortical layer II/III or spinal cord (Fig. 3C,D; Multiple *t*-test; $p = 0.001925$). Similarly, qPCR analyses revealed a significant decrease of *SOD1^{G37R}* transgene expression selectively within layer V of the cerebral cortex, and not in the layer II/III or the spinal cord (Fig. 3E; Multiple *t*-test; $p = 0.01834$). As expected, ablation of the *SOD1^{G37R}* transgene within the cortical layer V was not complete, given the selected expression of Cre recombinase in only a subpopulation of neurons, i.e. the SubCerePN, and not in other neuronal and glial populations, i.e. the excitatory callosal projection neurons, inhibitory interneurons, astrocytes, microglia and oligodendrocytes (Lodato et al., 2014). Together, the data suggest that our strategy to excise *SOD1^{G37R}* transgene from CSN, and more broadly SubCerePN and other CFuPN, is efficient.

3.4. Selective removal of *SOD1^{G37R}* from CSN prevents their neurodegeneration without affecting the surrounding reactive gliosis

Degeneration of the CSN is a hallmark of ALS and has been reported in different mutant *SOD1* mouse models of the disease (Marques et al., 2019; Ozdinler et al., 2011; Zang and Cheema, 2002). In the *Sod1^{G86R}* mouse line, we further demonstrated that lumbar-projecting CSN are more affected than the rest of the population, in accordance with an initial impairment of the hind limbs, and a somatotopic relationship between cortical and spinal neurodegenerations (Marques et al., 2019). To test whether *SOD1^{G37R}* excision from the CSN could impact their survival, we retrogradely labelled lumbar-projecting CSN by injecting the tracer FluoroGold into the lumbar part of the dorsal funiculus of *SOD1* and *CrymSOD1* animals, along with their control littermates WT and *CrymCre*. We performed the labelling at two different ages: symptomatic (11 months) and disease end-stage (14–16 months) (Fig. 4A). Microscopy analyses of lumbar projecting CSN revealed a significant loss of this neuronal population in *SOD1* animals compared to controls WT and *CrymCre* at a symptomatic stage (24.27 ± 8.16 % loss, $p = 0.037$) and at disease end-stage (21.79 ± 6.60 % loss, $p = 0.0096$) (Fig. 4B,C), indicating that *Floxed-SOD1^{G37R}* recapitulated CSN degeneration, like other mutant *SOD1* mouse lines. Excision of *SOD1^{G37R}* transgene from CSN and other CFuPN was sufficient to completely prevent the loss of CSN at both ages (*SOD1* vs *CrymSOD1*: $p = 0.027$ at symptomatic stage and $p = 0.027$ at disease end-stage; WT & *CrymCre* vs *CrymSOD1*: $p = 0.92$ at symptomatic stage and $p = 0.99$ at disease end-stage). In order to test whether the protection of CSN could positively impact other cortical pathological hallmarks of the disease, we performed immunolabellings on end-stage *SOD1* and *CrymSOD1* and their age-matched control littermates to reveal the astrogliosis marker GFAP, and the microgliosis marker IBA1 (Fig. 4D,F). Immunofluorescence analysis revealed an overall mild increase of GFAP and IBA1 immunoreactivity that appeared as discrete patches in *SOD1* and *CrymSOD1* compared to controls (Fig. 4D,F). Because increased GFAP and IBA1 immunoreactivity seemed more particularly restricted to the cortical layer V, we further quantified their intensities within this layer, along with the cortical layer II/III (Fig. 4E,G). We observed that GFAP immunoreactivity was not significantly different across genotypes within the cortical layer II/III. Contrastingly, *SOD1* and *CrymSOD1* animals presented a significantly higher GFAP immunoreactivity within the cortical layer V, in comparison with their WT and *CrymCre* littermates (*SOD1*: increase of 497 ± 53.68 % compared to WT & *CrymCre*, $p < 0.0001$; *CrymSOD1*: increase of 479 ± 53.68 % compared to WT & *CrymCre*, $p < 0.0001$), but no significant difference could be observed between *SOD1* and *CrymSOD1* animals ($p = 0.9394$) (Fig. 4E). Similarly, no difference in IBA1 immunoreactivity could be observed across genotypes within the cortical layer II/III, while increased immunoreactivity was present in cortical layer V of *SOD1* and *CrymSOD1* animals compared to WT & *CrymCre* (*SOD1*, $p = 0.0198$; *CrymSOD1*, $p = 0.0043$), without significant difference between *SOD1* and *CrymSOD1* animals ($p = 0.8738$) (Fig. 4F). Taken in their whole, the data suggest that *SOD1^{G37R}* expression by CSN is sufficient to induce their degeneration in a cell-autonomous manner. In addition, CSN degeneration and local (cortical layer V) reactive gliosis appear to be independent from each other: reactive gliosis is neither a cause nor a consequence of CSN degeneration. Together, the data indicate that selective genetic excision of the *SOD1^{G37R}* transgene from CSN is sufficient to prevent their degeneration, but does not impact the surrounding gliosis, demonstrating that CSN degeneration relies on cell-autonomous mechanisms.

3.5. Rescue of the CSN population limits spasticity

Degeneration of CSN (or upper motor neurons) leads to the development of the “upper motor neuron syndrome” characterized by decreased motor control, muscular weakness, altered muscle tone, clonus, spasticity and other manifestations of hyperreflexia (van Es

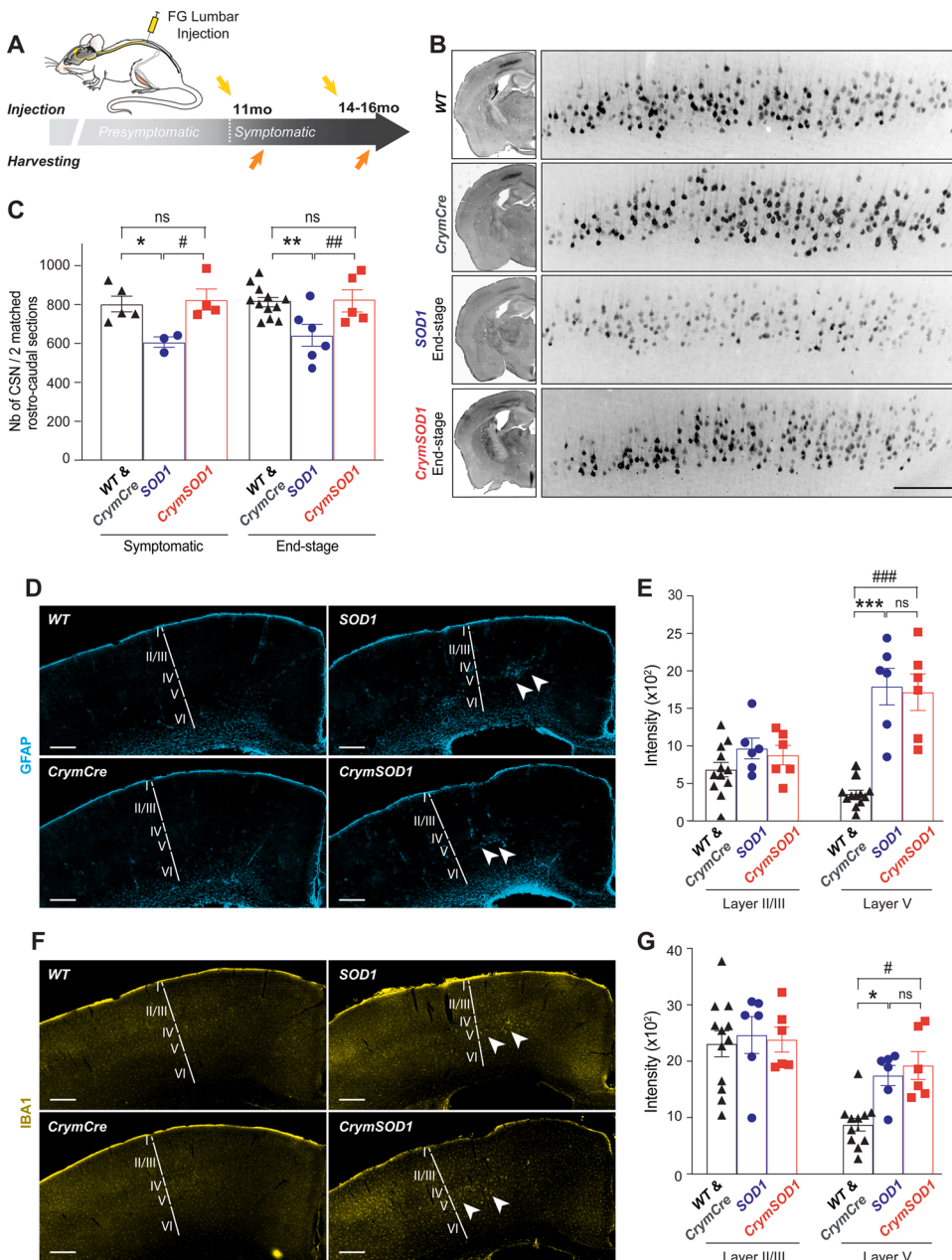


Fig. 4. Selective ablation of *SOD1*^{G37R} from SubCerePN prevents loss of CSN, but not reactive gliosis.

A. Schematic of the experimental strategy.

B. Representative negative fluorescence images of the brain hemisphere (left panels) and cerebral cortex (enlarged insets, right panels) of WT, *CrymCre*, *SOD1* and *CrymSOD1* mice showing CSN marked upon retrograde labelling with FG at disease end stage.

C. Bar graph presenting the quantification of FG-labelled CSN at symptomatic and disease end stage. N = 5 WT and *CrymCre*, 3 *SOD1* and 4 *CrymSOD1* at symptomatic stage and N = 12 WT and *CrymCre*, 6 *SOD1* and 5 *CrymSOD1* at disease end stage. * or # $p < 0.05$ and ** or ## $p < 0.01$ in 1-way ANOVA followed by a Tukey's multiple comparisons test.

D, F. Representative images of the cerebral cortex WT, *CrymCre*, *SOD1* and *CrymSOD1* mice showing GFAP (D, blue) and IBA1 (F, yellow) immunoreactivity at disease end stage.

E, G. Bar graphs representing the averaged intensity of GFAP (E) and IBA1 (G) signals in cortical layers II/III and V. N = 12 WT and *CrymCre*, 6 *SOD1* and 6 *CrymSOD1*. * or # $p < 0.05$, *** or ### $p < 0.001$ and ns: non-significant in 2-way ANOVA followed by Tukey's multiple comparisons test.

et al., 2017; Ivanhoe and Reistetter, 2004; Purves et al., 2004). To test whether maintenance of the CSN population could impact spasticity, we recorded the long lasting tail muscle activity following cutaneous stimulation in awake and fully paralyzed *SOD1* and *CrymSOD1* animals prior to harvesting (Bennett et al., 1999; Dentel et al., 2013; El Ouassini et al., 2017) (Fig. 5A-C). Within the *CrymSOD1* group, frequency of spastic mice was lower than within the *SOD1* group, but the difference did not reach significance ($p = 0.5963$, Fig. 5B), however, the amplitude of the response was significantly smaller within the *CrymSOD1* group than within the *SOD1* one ($p = 0.0452$), suggesting that *SOD1*^{G37R} excision from the CSN and maintenance of the CSN population was sufficient to limit spasticity (Fig. 5C).

In the *FloxedSOD1*^{G37R} mouse model, spasticity has previously been linked to serotonergic neuron degeneration in the raphe nuclei (Dentel et al., 2013; El Ouassini et al., 2017). We thus tested whether the decreased levels of spastic response that we recorded with the tail long lasting reflex could be at least partly attributed to degeneration of serotonergic neurons. We quantified the number of TPH2-positive

neurons present in the dorsal raphe nucleus (DR) and the median raphe and raphe magnus nuclei of end-stage *SOD1* and *CrymSOD1* and their control littermates, WT and *CrymCre* (Fig. 5D-F). We did not detect any difference in the median raphe and raphe magnus nuclei across genotypes (Fig. 5E,F). However, we observed a significant loss of TPH2-positive neurons of *SOD1* and *CrymSOD1* animals compared to WT & *CrymCre* animals in the dorsal raphe nucleus (*SOD1*: loss of 30.14 ± 6.02 , $p < 0.0001$ and *CrymSOD1*: loss of 35.98 ± 6.40 ; $p < 0.0001$, Fig. 5E,F). This loss was accompanied by an enlargement of the aqueduct in the *SOD1* and *CrymSOD1* mice compared to WT & *CrymCre* mice (Fig. 5E). However, no significant difference in the number of dorsal raphe nucleus TPH2-positive neurons could be observed between *SOD1* and *CrymSOD1* animals ($p = 0.7057$, Fig. 5F). Together, the data suggest that in the *FloxedSOD1*^{G37R} mouse line, intensity of the spastic tail long lasting reflex can be at least partly attributed to CSN dysfunction and/or degeneration, and not only to serotonergic neuron degeneration.

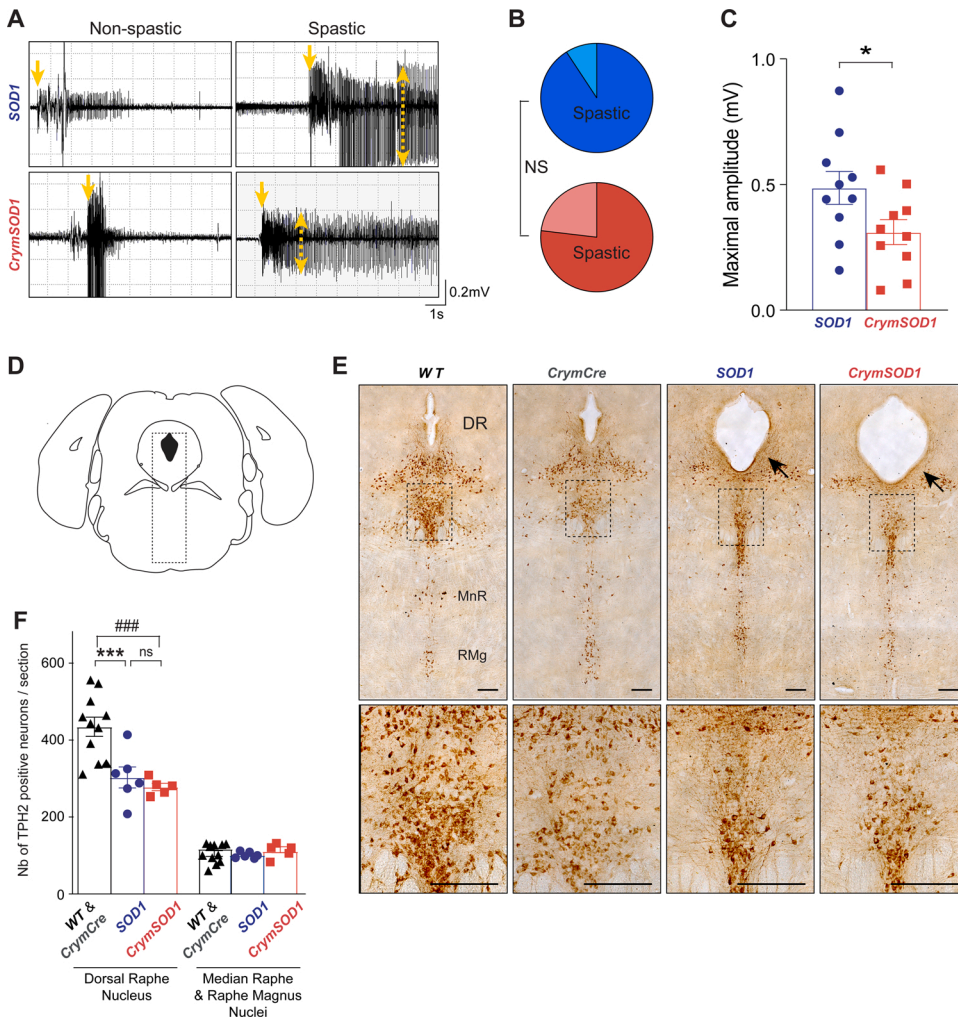


Fig. 5. Selective deletion of *SOD1*^{G37R} from CSN limits spasticity.

A. Representative EMG recordings of tail's muscle long lasting reflex (LLR) detected in end stage awake mice *SOD1* (N = 11), and *CrymSOD1* (N = 13) presenting a complete paralysis of hind limbs. Spasticity-related tail LLR is observed upon stimulation (yellow single head arrows) in subgroups of animals, and amplitude of the response can be recorded (yellow single head arrows).

B. Pie charts representing the frequency of animals with a tail LLR amongst the *SOD1* (light blue: not spastic, dark blue: spastic) and *CrymSOD1* mice (light red: not spastic, dark red: spastic). Difference between the two genotypes is not significant, Fischer's exact test.

C. Graph bar representing the LLR maximal amplitudes for spastic *SOD1* (N = 10) and *CrymSOD1* (N = 10) mice. Student unpaired *t*-test.

D. Schematic of the coronal section selected for TPH2-positive neurons labeling and counting (Bregma -4.84 mm). **E** Representative images of TPH2 immunoreactivity in the brainstem of end stage mice. (DR: dorsal raphe, MnR: median raphe, RMg raphe magnus). Arrowheads indicate the enlargement of the aqueduct (Sylvius) in *SOD1* and *CrymSOD1* animals compared to WT and *CrymCre* control animals. Scale bars 200 μm. **F** Bar graph representing the average number of TPH2-positive neurons in the dorsal raphe nucleus and the median raphe and raphe magnus nuclei respectively. N = 12 WT and *CrymCre*, 6 *SOD1* and 5 *CrymSOD1*. 2-way ANOVA followed by a Tukey's multiple comparisons test. **p* < 0.05, *** or ### *p* < 0.001 and ns: non-significant.

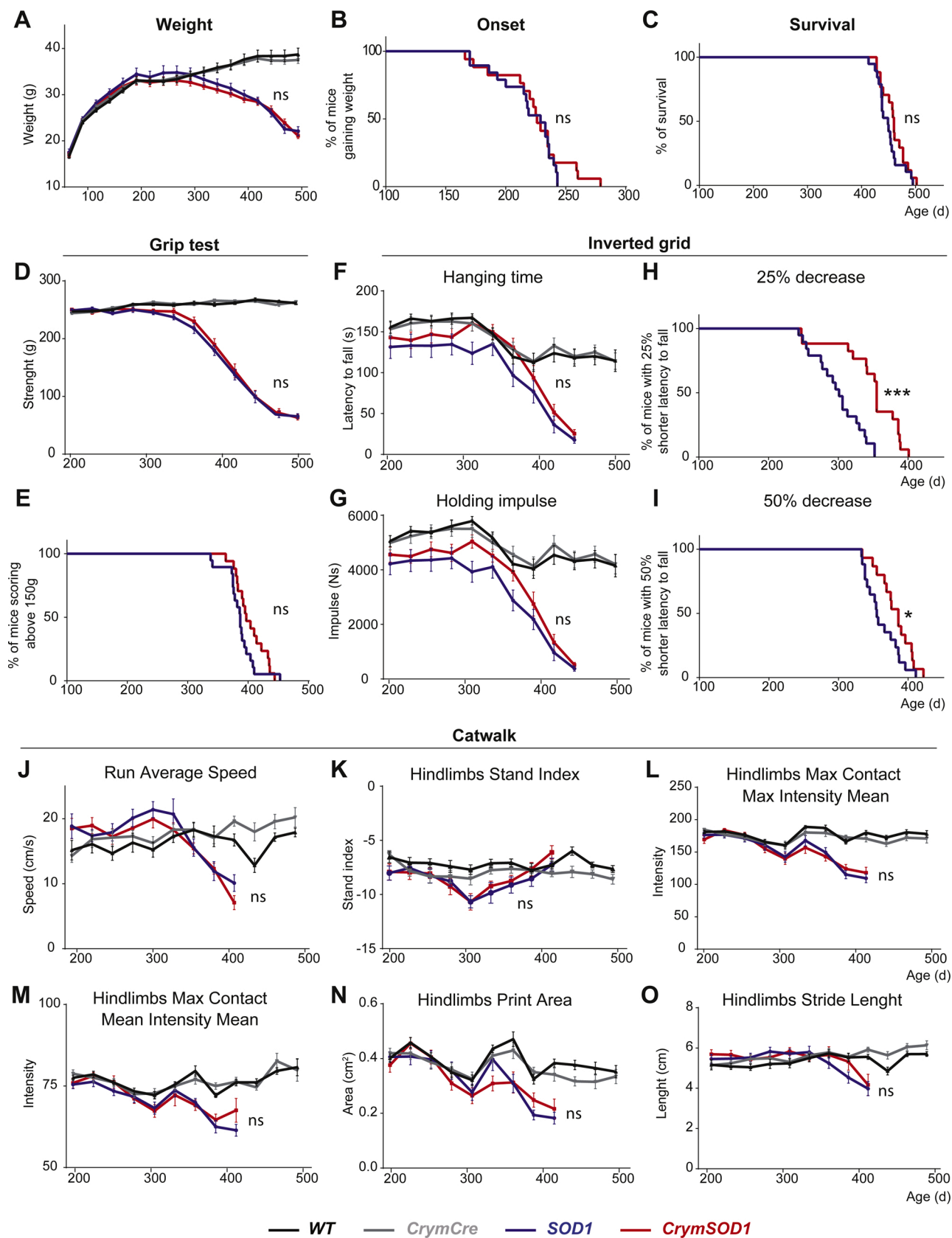
3.6. Maintenance of the CSN population does not impact ALS-like symptoms onset and progression

Next, we sought to test the effect of CFuPN-selective ablation of *SOD1*^{G37R} on the manifestation of ALS-like symptoms in our mice, i.e. weight loss, disease onset, premature death and motor impairment (Fig. 6). As already reported (Boillee et al., 2006), *SOD1* mice stopped gaining weight (Fig. 6A), started progressively losing weight from 160 days on (disease onset, Fig. 6B), and died prematurely from 410 days on (Fig. 6C). Both *CrymSOD1* and their *SOD1* littermates showed similar pattern of weight evolution over time (Fig. 6A; *p* = 0.4383), we did not detect any difference between *SOD1* and *CrymSOD1* animals regarding disease onset (Fig. 6B; *p* = 0.4527B) and survival (Fig. 6C; *p* = 0.2152). Motor performance analyses revealed no difference between the *SOD1* and *CrymSOD1* groups regarding the evolution of the grip strength of the animals (Fig. 6D; *p* = 0.5028), or the time when it started decreasing (Fig. 6E; *p* = 0.1114). Although, *CrymSOD1* animals did perform similarly to their *SOD1* littermates on the inverted grid test, in terms of latency to fall and holding impulse (Fig. 6F, *p* = 0.2112; 6 G, *p* = 0.1825), we detected a delay of the age at which animals had lost 25 % or 50 % of their initial latency to fall (Fig. 6H, *p* < 0.0001; 6I, *p* = 0.0335). Contrastingly, Catwalk analyses of the gait revealed no difference between *SOD1* and *CrymSOD1* animals regarding the run average speed, the hind limbs "stand index", "max contact max intensity mean", "max contact mean intensity mean", "print area" and "stride length" (Fig. 6J, *p* = 0.6343; 6 K *p* = 6064; 6 L, *p* = 9282; 6 M, *p* = 3961; 6 N, *p* = 0.9503; 6O, *p* = 0.5844). In their whole, the data indicate that deletion of

SOD1^{G37R} from the CFuPN and maintenance of the CSN population ameliorate discrete motor functions without affecting disease onset and survival.

3.7. Maintenance of the CSN population does not prevent or delay muscle denervation or spinal pathology

Next, we tested whether ablation of the *SOD1*^{G37R} transgene from the CSN and related CFuPN impacted muscular and spinal manifestations of the disease. We first ran electromyographic recordings on the gastrocnemius and tibialis muscles of both hind limbs of end-stage *SOD1* and *CrymSOD1* animals and their WT and *CrymCre* age-matched control littermates (Fig. 7A,B). Innervated muscles were given a score of 0, denervated muscles a score of 1 and the sum of the scores of the four muscles was calculated for each animal (Fig. 7B). Denervation was clearly observed in *SOD1* and *CrymSOD1* mice compared to the WT and *CrymCre* controls, but no significant difference was observed between *SOD1* and *CrymSOD1* mice (*p* = 0.0809; Fig. 7B). To further assess the innervation status of the muscles, we labelled the neuromuscular junctions (NMJ) of the tibialis anterior muscle of end-stage *SOD1* and *CrymSOD1* mice and controls WT and *CrymCre* (Fig. 7C). Rating of the NMJ integrity into three categories - innervated, partly denervated and fully denervated - confirmed the vast denervation of the *SOD1* and *CrymSOD1* muscles compared to controls, and indicated that *SOD1* and *CrymSOD1* animals presented similar levels of denervation (*p* = 0.9474, Fig. 7D). In accordance with this result, qPCR analyses of the tibialis anterior muscle revealed important up-regulation of the expression of



(caption on next page)

Fig. 6. CSN rescue does not impact disease onset or survival.

A. Graphical representation of the longitudinal follow up of the body weight for all genotypes.
 B, C. Kaplan-Meier plots of disease onset (age when animals reach their weight peak) and survival (age at death) in days, for *SOD1* (blue) and *CrymSOD1* mice (red). ns: non significant, Log-rank test (Mantel-Cox).
 D, E. Graphical representations of the evolution of the grip strength of the animals over time (D), and Kaplan-Meier representation of the percentage of animals presenting a grip strength above 150 g (E).
 F, G, H, I. Graphical representations of the latency to fall from an inverted grid (F) and the corresponding holding impulse (G) and Kaplan-Meier representations of the percentage of animals that still present at least 75 % (H) or 50 % of their initial latency (I) on that same test.
 J, K, L, M, N, O. Graphical representations of selected gait parameters recorded on CatWalk. For all data, WT (N = 20), *CrymCre* (N = 20), *SOD1* (N = 15), and *CrymSOD1* (N = 14). Data were analyzed by two-way anova (A, D, F, G, J-O) or log rank Mantel-Cox (B, C, E, H, I) * $p < 0.05$, *** $p < 0.001$, ns: non-significant.

the gamma subunit of the acetylcholine receptor (*AchR γ*), a typical molecular marker of denervation, in end-stage *SOD1* and *CrymSOD1* mice compared to controls (*SOD1* vs controls, $p = 0.0418$; *CrymSOD1* vs controls, $p = 0.046$; *SOD1* vs *CrymSOD1* $p = 0.5730$; Fig. 7E). Similarly, quantification of the MN present in the 5th segment of the lumbar spinal cord upon toluidine blue labelling indicated an important loss of MN in *SOD1* and *CrymSOD1* animals compared to control with a similar extent for *SOD1* and *CrymSOD1* mice (Fig. 7F,G; $p = 0.9929$). Spinal MN degeneration upon *SOD1*^{G37R} overexpression in *SOD1* and *CrymSOD1* mice was accompanied with aggregation of human misfolded SOD1 protein and p62 (Fig. 8A,B). Quantification of the fluorescence intensity revealed similar extents of pathology between *SOD1* and *CrymSOD1* animals, both in the white and grey matters (Fig. 8A,B). To further test whether *SOD1*^{G37R} excision from the CSN could affect the levels of mutant SOD1 protein in their targeted tissue, we compared the relative proportions of soluble and insoluble human misfolded SOD1 protein (Fig. 8C,D), along with the proportion of total (soluble and insoluble) misfolded SOD1 protein over total spinal cord proteins (Fig. 8E). We did not detect any difference between *SOD1* and *CrymSOD1* animals: both genotypes had similar amounts of misfolded human SOD1 protein amongst the whole spinal cord proteins (Fig. 8E), and in similar proportions between soluble and insoluble fractions (Fig. 8D). Finally, to test, whether *SOD1*^{G37R} excision from the CSN could ameliorate astrogliosis and microgliosis, we performed immunolabellings of GFAP, IBA1 respectively (Fig. 8F,G). Quantification of the fluorescence intensity of these different pathology markers revealed again similar extents of pathology between *SOD1* and *CrymSOD1* animals, both in the white and grey matter (Fig. 8F,G) with the exception of GFAP that appeared less intense in the white matter of *CymSOD1* mice than in *SOD1* mice ($p = 0.0213$; Fig. 8G). Together, the data thus rule out the possibility of the transmission of significant amounts of misfolded human SOD1 protein by the CSN to their spinal targets, and indicate that while genetic ablation of *SOD1*^{G37R} from the CFuPN is beneficial to CSN survival, it has virtually no impact on MN survival and spinal pathology.

4. Discussion

In the present study, we sought to determine i) how cell-autonomous expression of a mutant toxic transgene could impact CSN survival, and ii) whether corticofugal disease propagation relied on the transmission of misfolded mutant proteins by the CFuPN to their targets. We demonstrated that genetic ablation of the mutant *SOD1*^{G37R} transgene from CFuPN was sufficient to maintain the whole population of CSN, but had no effect on mutant SOD1 amounts and aggregate burden in the spinal cord, nor on other spinal pathological hallmarks, MN survival, disease onset and survival. Together, the data provide insights into the mechanisms that underlie CSN degeneration and the possible mechanism of corticofugal propagation of the disease in the context of ALS.

4.1. A new Cre mouse line restricted to CFuPN

To target CFuPN, we generated a new Cre recombinase mouse line by inserting the tamoxifen-inducible *CreER*^{T2} transgene downstream of the *Crym* promoter and coding sequence. This strategy allowed to spatially restrict Cre expression to CFuPN, along with a discrete population of

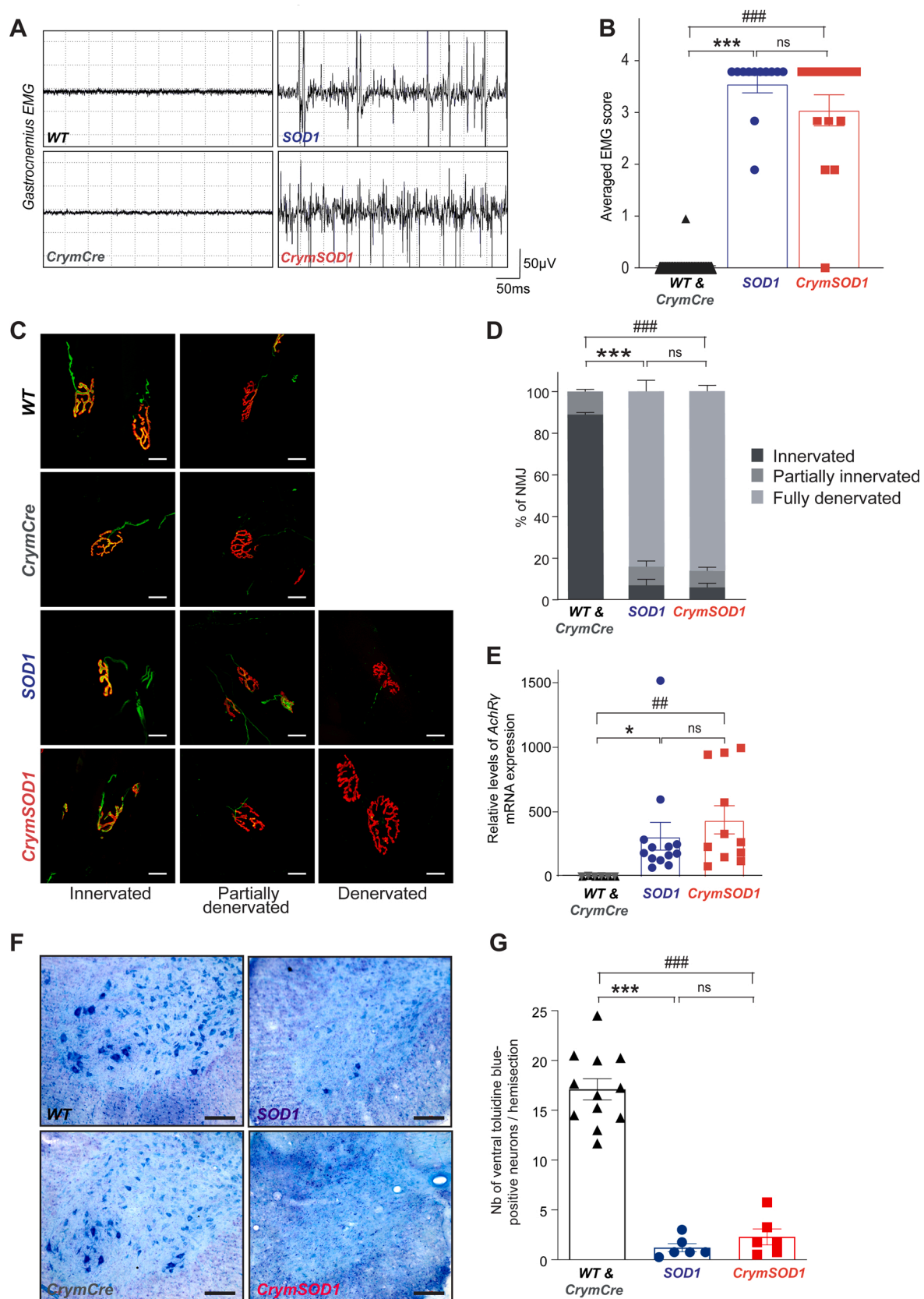
neurons in the dorsomedial part of the globus pallidus whose identity remains to be determined, and to temporally restrict Cre-expression upon Tamoxifen injection. Cre expression fully recapitulated *Crym* expression and proved efficient to target CSN and CFuPN. In future studies, the *CrymCreER*^{T2} mouse line could prove useful to perform similar rescue experiments when crossed for instance with the new *Fus*^{Δ^{NLS}} mice (Scekcic-Zahirovic et al., 2017), or complementary gain-of-function experiments, when injected with viruses encoding Cre-inducible transgenes of *SOD1*, *TARDBP*, *FUS* or *C9ORF72* genes, all relevant to ALS, but also potentially of *ALTI*, *SPAST*, *HSPD1*, *SPG7* or *KIF5A*, all relevant to hereditary spastic paraplegia, a neurodegenerative disease that selectively affects CSN without impairing MN survival (Strong and Gordon, 2005). The temporal activation of *CreER*^{T2} further allows testing the impact of these genes, or of their removal, at different moment of the life of the animals, allowing for instance to test pre-symptomatic versus symptomatic approaches. Finally, within the field of neurodegeneration, but also within the much broader field of neuroscience, *CrymCreER*^{T2} mice could further be used for optogenetic or chemogenetic approaches in order to better understand the role of CFuPN activity on the overall cortical circuit, but also on targeted circuits, such as those of the spinal cord, pons, superior colliculus or thalamus for instances. Because *Crym* expression is rather late during the differentiation of CFuPN (Arlotta et al., 2005), *CrymCreER*^{T2} mice may not be the most appropriate line to study the generation and early specification of CFuPN, however, other elegant temporally inducible Cre and Flp mouse lines exist that allow combinatorial targeting of major cortical progenitor types and CFuPN subclasses (Matho et al., 2020).

4.2. Floxed *SOD1*^{G37R} mice recapitulate loss of CSN

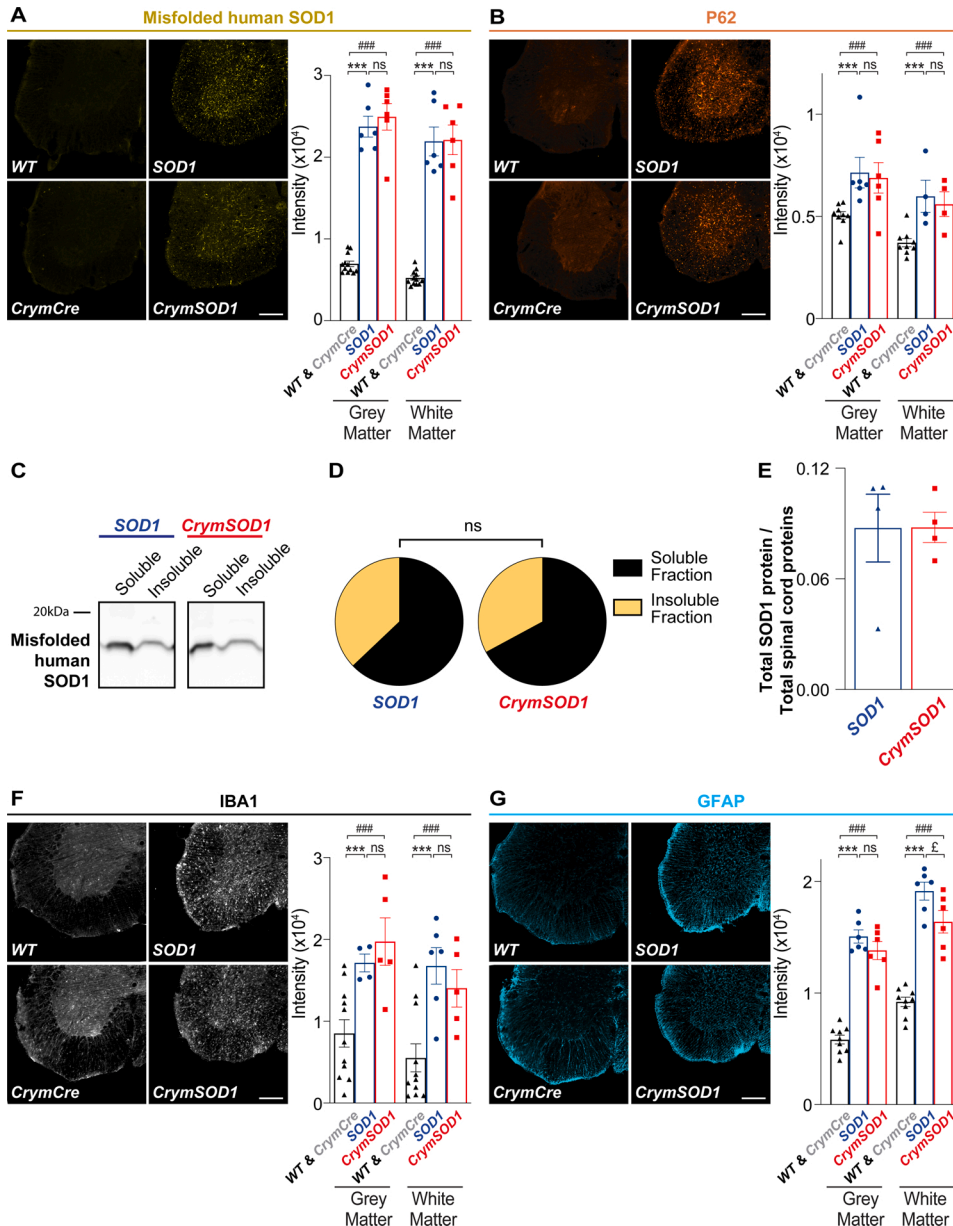
In human, progressive degeneration of the CSN translates into a series of symptoms grouped under the term of upper motor neuron syndrome, a hallmark of the clinical manifestation of ALS (Ivanhoe and Reistetter, 2004; Purves et al., 2004). Post mortem analyses of the motor cortex of ALS patients confirmed the loss of CSN, or Betz cells (Charcot, 1874; Nihei and Kowall, 1993). Similarly numerous rodent models of the disease recapitulate CSN or layer V SubCerePN degeneration such as the *C9-BAC* mice (Liu et al., 2016), the *hPFN1*^{G118V} mice (Fil et al., 2016), the *TDP43*^{A315V} mice (Herdewyn et al., 2014; Wegorzewska et al., 2009), the *TDP43*^{G298S} mice (Ebstein et al., 2019), the *SOD1*^{G93A} rats (Thomsen et al., 2014), and *SOD1* mouse models (Marques et al., 2019; Ozdinler et al., 2011; Yasvoina et al., 2013; Zang and Cheema, 2002). In the *Sod1*^{G86R} mouse model, we further demonstrated that CSN loss starts long before first signs of MN degeneration can be observed, and that CSN and MN degeneration are somatotopically related (Marques et al., 2019). In this model, lumbar-projecting CSN are affected earlier than the rest of the population, similarly to lumbar MN being affected earlier than the rest of the population. Here, by sampling the subpopulation of lumbar-projecting CSN, we demonstrated that the *FloxedSOD1*^{G37R} mice recapitulate CSN degeneration as well.

4.3. Cell-autonomous mechanisms of CSN degeneration

Genetic ablation of the *SOD1*^{G37R} transgene was sufficient to prevent loss of CSN, suggesting that CSN degeneration relies on cell-autonomous



(caption on next page)

Fig. 7. Improved survival of CSN does not prevent denervation nor MN degeneration.**A.** Traces of EMG recording of the gastrocnemius muscle of end staged, deeply anaesthetized *SOD1* and *CrymSOD1* animals.**B.** Bar graph presenting the EMG score calculated for *SOD1* and *CrymSOD1* mice. $N = 20$ WT, 18 *CrymCre*, 12 *SOD1* and 14 *CrymSOD1*. *** $p < 0.001$ and ns: non-significant in 1-way ANOVA followed by a Tukey's multiple comparisons test.**C.** Representative maximum intensity projection images of z-stacks of typically innervated, partially or fully denervated neuromuscular junctions (NMJ) from end-stage *SOD1* and *CrymSOD1* mice and their age-matched WT and *CrymCre* littermates.**D.** Bar graph representing the average proportions of innervated (dark grey), partly denervated (medium grey) and fully denervated (light grey) NMJ for each genotype; 2-way ANOVA followed by Tukey multiple comparisons test; $N = 6$ animals per genotype. *** $p < 0.001$ and ns: non-significant. Scale bars $20 \mu\text{m}$.**E.** Bar graph representing qPCR analyses of the *AchR γ* (gamma) mRNA expression levels in *SOD1* (blue) and *CrymSOD1* (red) mice. $N = 6$ per genotype. * $p < 0.05$, ** $p < 0.01$ and ns: non-significant in 1-way ANOVA followed by a Tukey's multiple comparisons test.**F.** Representative images of toluidine blue staining of L5 spinal cord sections from end-stage *SOD1*, and *CrymSOD1* mice and control WT, *CrymCre* animals. Scale bars $100 \mu\text{m}$.**G.** Bar graphs showing mean numbers of spinal motor neuron per hemi-section for all genotypes. $N = 6$ per genotype. *** or ### $p < 0.001$ and ns: non-significant in 1-way ANOVA followed by a Tukey's multiple comparisons test.**Fig. 8.** Improved survival of CSN does not modify key pathological hallmarks of ALS in the spinal cord.**A, B, F, G.** Left Panels: representative immunofluorescence images of spinal cord hemisections showing misfolded human SOD1 (SOD1, yellow, A) or P62- (orange, B) positive aggregates, and IBA1 (white, E) and GFAP (cyan, F) protein expression in end stage *SOD1*, and *CrymSOD1* mice and their age-matched WT and *CrymCre* littermates. Scale bar $200 \mu\text{m}$. Right panels: Bar graphs representing the average intensity of misfolded human SOD1- (A), P62- (B), IBA1- (F) and GFAP- (G) specific signals in the grey and white matter of the spinal cord. * $p < 0.05$, *** or ### $p < 0.001$ and ns: non-significant in 2-way ANOVA followed by Tukey's multiple comparisons test.**C.** Representative immunoblots for misfolded human SOD1 protein detected in the soluble and insoluble fractions of homogenates from the spinal cord of end-stage *SOD1* and *CrymSOD1* mice. $N = 4$ animals per genotype.**D.** Pie charts representing the relative proportions of misfolded human SOD1 protein present in the soluble and insoluble fractions of homogenates from the spinal cord of end-stage *SOD1* and *CrymSOD1* mice. $N = 4$ animals per genotype. Student unpaired t-test, ns: non-significant.**E.** Bar graph representing the relative proportion of total misfolded human SOD1 protein (soluble and insoluble) in total spinal cord proteins, showing no difference between *SOD1* and *CrymSOD1* mice.

mechanisms and is independent from its *SOD1*^{G37R}-expressing environment, i.e. other excitatory and inhibitory neurons, astrocytes, microglia, oligodendrocytes located in the motor cortex but also along the corticospinal tract and in the spinal cord. The data thus indicate that CSN

degeneration strictly relies on cell-autonomous mechanisms. Similar cell-autonomous mechanisms were described for the brainstem serotonergic neurons (El Oussini et al., 2017), but not for the spinal MN whose degeneration relies instead on the combination of cell-autonomous and

non-cell autonomous mechanism (Ilieva et al., 2009; Lee et al., 2016; Serio and Patani, 2017). Thus, *SOD1*^{G37R} transgene expression differentially affects neuronal survival depending on the nature of the neuronal population. Interestingly, reactive astrogliosis and microgliosis were very moderate in the motor cortex of the *FloxedSOD1*^{G37R} animals in comparison with their spinal cord. Cortical astrogliosis appeared as discrete patches, while microgliosis rather corresponded to a two-fold increase of IBA1 expression, and these were selectively found in the layer V of the motor cortex where CSN reside. Surprisingly, maintenance of the CSN population by selective removal of the *SOD1*^{G37R} transgene had no impact on reactive gliosis, suggesting that astrogliosis and microgliosis were not secondary to CSN degeneration. Similarly, occurrence of astrogliosis and microgliosis in the cortical layer V of the *CrymSOD1* animals at similar levels than in the *SOD1* animals did not prevent the cell-autonomous beneficial effect of *SOD1*^{G37R} ablation on CSN survival, suggesting that CSN degeneration is not secondary to reactive gliosis either. Overall, this suggests that CSN degeneration and cortical reactive gliosis may be independent from each other. The precise co-localization, within the cortical layer V, of CSN degeneration and reactive gliosis is nevertheless quite remarkable, and contribution of reactive glia to CSN dysfunction remains a possibility. The discrepancy between cortical and spinal glial contribution to neighbouring CSN and MN survival respectively may arise from the level of gliosis itself, rather moderate in the cerebral cortex and important in the spinal cord, or from the actual nature of the targeted neuronal populations. Together, the data strongly suggest that the mechanisms that govern MN degeneration may not be directly transposable to CSN degeneration, and that investigating how CSN degenerate, as we recently started (Marques et al.,

2019), may provide new insights into ALS pathogenesis and potentially new therapeutic avenues.

4.4. Contribution of CFuPN to disease onset and progression

A growing number of neurophysiological and pathological studies suggest a cortical origin of ALS (Eisen et al., 2017; Geevasinga et al., 2016) and recent longitudinal imaging analyses support a propagation of impairments along the corticofugal tracts (Kassubek et al., 2014; Verstraete et al., 2013). Using mouse genetics, we recently provided the first experimental evidence of the corticofugal hypothesis by showing that absence of SubCerPN, the most important output of the cerebral cortex, delayed disease onset and extended survival in the *Sod1*^{G86R} mouse model of the disease (Burg et al., 2020) (Fig. 9). A few years ago, Thomsen and colleagues knocked-down the *SOD1*^{G93A} transgene in the posterior motor cortex of transgenic rats (Thomsen et al., 2014), using an AAV9 virus that selectively transduced neurons. This strategy delayed disease onset and extended survival (Fig. 9), but whether the beneficial effect was reached upon targeting excitatory projection neurons (including CFuPN) or inhibitory interneurons (INs), or both remained an open question. Our study indicated that selective removal of *SOD1*^{G37R} transgene from excitatory CFuPN does not impact disease onset and survival (Fig. 9). Taken together, these studies suggest that improved mouse survival can be achieved either upon complete removal of the CFuPN, or upon genetic correction of all cortical neurons, i.e. CFuPN but also excitatory callosal projection neurons and inhibitory interneurons (Fig. 9).

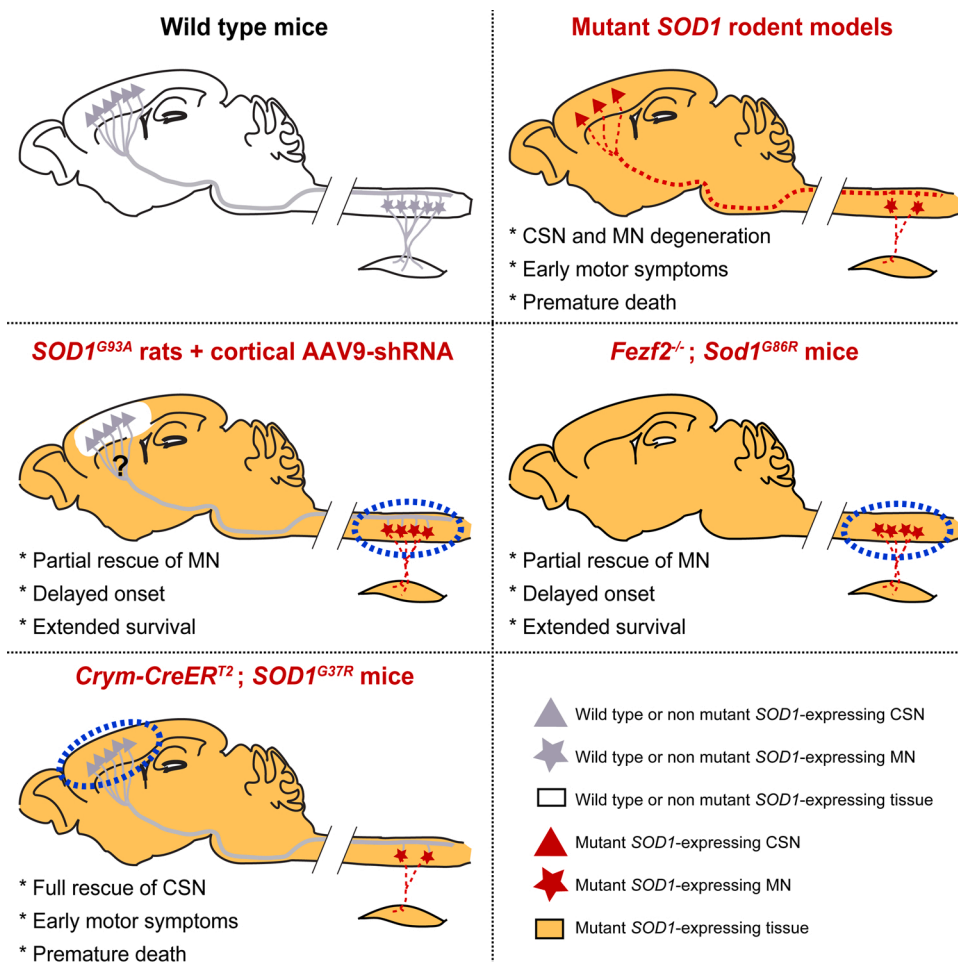


Fig. 9. Complementary genetic manipulations of the CFuPN allow unravelling their contribution to ALS.

Schematic representation of the rodent central nervous system and its populations of CSN/CFuPN (triangles) and spinal MN (stars). Both populations and their axons are healthy in the wild-type animal (top left). Ubiquitous mutant *SOD1* expression (orange and red) leads to the combined degeneration of CSN and MN. Knock-down of the *SOD1*^{G93A} transgene in the posterior motor cortex of transgenic rats using an AAV9-shRNA promoted CSN survival, protected MN, delayed disease onset and increased survival (Thomsen et al., 2014) (middle left panel). Similarly, genetic ablation of the CSN/CFuPN protected MN, delayed disease onset and increased survival of the *Sod1*^{G86R} mouse model of the disease (Burg et al., 2020) (middle right panel). Contrastingly, selective genetic ablation of the *SOD1*^{G37R} transgene from the CSN/CFuPN prevented CSN degeneration without improving MN survival or disease progression (this study) (bottom left panel). Together, the data indicate that total absence of CSN/CFuPN, or broad genetic correction of the cortical neuronal populations (excitatory including CFuPN and inhibitory using and AAV9-shRNA) is more beneficial than the maintenance of wild-type like CSN/CFuPN, suggesting that, when maintained in a mutant environment, wild-type like CSN/CFuPN continue to spread disease from the motor/cerebral cortex to its targets.

4.5. Mechanisms of corticofugal propagation

While the studies from Thomsen and colleagues and Burg and colleagues support the idea of a corticofugal dissemination of the disease (Burg et al., 2020; Thomsen et al., 2014), they do not inform on the underlying mechanisms. Two possibilities have been proposed: a prion-like transmission of misfolded proteins (Braak et al., 2013; McAlary et al., 2019; Prasad et al., 2019) and a cortical hyperexcitability leading to altered neuronal excitability of CFuPN and subsequent excitotoxicity onto their targets (Eisen et al., 2017; Vucic and Kiernan, 2017).

The vast majority of ALS patients present intracellular inclusions of hyperphosphorylated and misfolded TDP-43 protein (Neumann et al., 2006), with the exception of *SOD1*-ALS patients and *FUS*-ALS patients that present inclusions positive for SOD1 and FUS respectively (Mackenzie et al., 2007; Munoz et al., 2009). Similarly to *SOD1*-ALS patients, *Sod1*^{G86R} animals do not display TDP-43 pathology (Burg et al., 2020). While the presence of TDP-43 pathology has not been tested in the *SOD1*^{G37R} mice, it is likely that these animals do not present any TDP-43 aggregates either, similarly to *SOD1*-ALS patients and *Sod1*^{G86R} mice. However, *SOD1*^{G37R} expression is sufficient to induce the formation of misfolded SOD1 aggregates in mice (Maier et al., 2018), and our data show that floxed *SOD1*^{G37R} mice also display SOD1-positive aggregates. However, these aggregates were not uniformly present within the CNS. Indeed, our data indicate that the brain, and the cerebral cortex in particular, remained virtually devoid of aggregates in comparison with the brain stem and spinal cord. Interestingly, smaller proteinopathy burden in the brain compared to the spinal cord was recently reported for *SOD1*-ALS patients (Nolan et al., 2020), highlighting the relevance of our observations to the human pathology. In addition, we observed that in the cerebral cortex of *SOD1*^{G37R} mice, misfolded human SOD1 protein remained mostly soluble. This opens the possibility that soluble misfolded SOD1 protein could be transmitted from one neuronal type to another along axonal projections, in accordance with a possible prion-like corticofugal propagation of ALS, as suggested (Braak et al., 2013). Our data indicate that mutant *SOD1*^{G37R} transgene genetic excision and subsequent mutant SOD1 protein removal from the CSN did not diminish the amount of total SOD1 protein in the spinal cord, nor its propensity to aggregate, indicating that spinal SOD1 soluble and insoluble proteins and aggregates essentially arise from the expression of the mutant *SOD1*^{G37R} transgene by spinal cell types (neurons and glia), and that if mutant SOD1 protein is released by CSN, this does not account for a significant proportion of total spinal SOD1 proteins, and has virtually no impact on MN survival and other spinal pathological hallmarks. While inter-cellular prion-like spread of misfolded proteins among spinal cells remains a possible event in ALS, our data rule out the possibility that corticofugal disease propagation relies on misfolded SOD1 proteins spread from CSN to their spinal targets.

Similarly to other neurodegenerative diseases that target different brain structures, ALS is characterized by early cortical hyperexcitability (Vucic and Kiernan, 2006), which has been proposed to induce glutamatergic excitotoxicity (Eisen et al., 2017; Vucic and Kiernan, 2017). Transcranial magnetic stimulation (TMS) studies demonstrated that cortical hyperexcitability develops prior to clinical onset in *SOD1* mutation carriers (Menon et al., 2015; Vucic et al., 2008) and negatively correlates with disease progression (Shibuya et al., 2016). Cortical hyperexcitability arises from both increased excitation and decreased inhibition, suggesting that both excitatory and inhibitory components are involved in this broad cortical circuit dysfunction (Brunet et al., 2020; Gunes et al., 2020). While cortical hyperexcitability has not been demonstrated by TMS in mouse models of the disease, several of them display cortical excitatory and inhibitory neurons dysfunctions that demonstrate cortical circuit imbalance reminiscent of the cortical hyperexcitability observed in patients (Brunet et al., 2020; Gunes et al., 2020). Cell-type specific manipulation of gene expression within selected cortical neuronal subtypes recently demonstrated the relevance

of cortical circuit dysfunction in ALS onset and progression. In the *TDP-43*^{A315T} mouse model of ALS, Zhang and collaborators demonstrated that parvalbumin (PV)-positive INs were hypoactive, while somatostatin (SST)-positive INs were hyperactive (Zhang et al., 2016), and that hyperactivity of SST-positive INs was responsible for hypoactivity of PV-positive INs, and in turn for hyperexcitability of layer V SubCerePN. Normal excitability of SubCerePN could be restored upon genetic ablation of SST-positive INs, and alleviated neurodegeneration (Zhang et al., 2016). Hypoactivity of PV-positive INs was also demonstrated in the *SOD1*^{G93A} mouse model of ALS (Khademullah et al., 2020). Chemo-genetic activation of the PV-positive INs in the motor cortex of *SOD1*^{G93A} mice resulted in decreased excitability of layer V excitatory neurons (SubCerePN, including CNS), delayed disease onset and improved motor functions and survival (Khademullah et al., 2020). These studies are the first to establish a clear link between dysfunction of the motor cortical circuits and disease onset and progression, and favour the possibility that corticofugal disease propagation in ALS could be mediated by altered excitability and activity of CFuPN.

Cortical hyperexcitability and altered CFuPN excitability and activity were proposed to induce glutamatergic excitotoxicity to their downstream targets in the spinal cord (Eisen et al., 2017; Vucic and Kiernan, 2017). But another, non-mutually exclusive scenario may exist. Recent work by Weskamp and colleagues elegantly demonstrated that neuronal hyperexcitability was sufficient to induce cytoplasmic accumulation of TDP-43 (Weskamp et al., 2019), linking for the first time hyperexcitability and pathology, and emphasizing the earliness of hyperexcitability in the cascade of pathogenic events that characterize ALS. This scenario could also explain the spread of the TDP-43 pathology to the structures receiving direct corticofugal connections (Brettschneider et al., 2014). It would thus be particularly informative to determine the consequences of the restoration of proper cortical excitability on the spinal pathology burden.

In light of these studies, the lack of beneficial effect of CFuPN genetic correction on motor symptoms onset and survival in mice that we report in this study could be interpreted as the result of the maintenance of altered cortical circuit dysfunction, maintenance of the corticospinal tract and maintenance of altered CSN excitability and activity in a non-cell autonomous manner. Contrastingly, beneficial effects from the genetic ablation of the CSN (Burg et al., 2020), or from the decreased excitability of CSN (Khademullah et al., 2020) could be interpreted as successful ways to prevent aberrant descending excitatory inputs onto spinal targets. Selective silencing of the CFuPN may in the future contribute to a better understanding of the role of cortical hyperexcitability in ALS, and potentially unravel new therapeutic targets.

Funding

The work has been supported by a European Research Council (ERC) starting grant #639737, a Marie Skłodowska-Curie career integration grant #618764, an "Association Française contre les Myopathies" (AFM)-Telethon trampoline grant #16923, a Neurex grant and a "Fédération pour la Recherche sur le Cerveau" (FRC) grant to CR. JCZ was supported by a post-doctoral fellowship from the AFM-Telethon #21993, TB by a PhD fellowship from the French Ministry of Research, and CM by a PhD fellowship from Inserm and Région Alsace.

Author contribution

JSZ and CR designed the research study, analysed the data and wrote the manuscript. JSZ, MF, GSL, TB, CM, JG and SDG conducted the experiments, acquired and analysed the data. MCB designed the *Crym-CreER*^{T2} mice and PK designed image analysis pipelines.

Declaration of Competing Interest

The authors declare that no competing interests exist.

Acknowledgments

The authors are extremely thankful to Annie Picchinenna and Marie-José Ruivo for technical assistance, and to Luc Dupuis and Denis Jabaudon for critical reading of the manuscript, and insightful comments.

Appendix A. The Peer Review Overview and Supplementary data

The Peer Review Overview and Supplementary data associated with this article can be found in the online version, at doi:<https://doi.org/10.1016/j.pneurobio.2020.101972>.

References

- Abbott, A., 2014. The changing face of primate research. *Nature* 506, 24–26.
- Arlotta, P., Molyneaux, B.J., Chen, J., Inoue, J., Kominami, R., Macklis, J.D., 2005. Neuronal subtype-specific genes that control corticospinal motor neuron development in vivo. *Neuron* 45, 207–221.
- Bennett, D.J., Gorassini, M., Sanelli, L., Han, Y., Cheng, J., 1999. Spasticity in rats with sacral spinal cord injury. *J. Neurotrauma* 16, 69–84.
- Boillee, S., Yamanaka, K., Lobsiger, C.S., Copeland, N.G., Jenkins, N.A., Kassiotis, G., Kollias, G., Cleveland, D.W., 2006. Onset and progression in inherited ALS determined by motor neurons and microglia. *Science* 312, 1389–1392.
- Braak, H., Brettschneider, J., Ludolph, A.C., Lee, V.M., Trojanowski, J.Q., Del Tredici, K., 2013. Amyotrophic lateral sclerosis—a model of corticofugal axonal spread. *Nat. Rev. Neurol.* 9, 708–714.
- Brettschneider, J., Del Tredici, K., Toledo, J.B., Robinson, J.L., Irwin, D.J., Grossman, M., Suh, E., Van Deerlin, V.M., Wood, E.M., Baek, Y., Kwong, L., Lee, E.B., Elman, L., McCluskey, L., Fang, L., Feldengut, S., Ludolph, A.C., Lee, V.M.Y., Braak, H., Trojanowski, J.Q., 2013. Stages of pTDP-43 pathology in amyotrophic lateral sclerosis. *Ann. Neurol.* 74, 20–38.
- Brettschneider, J., Arai, K., Del Tredici, K., Toledo, J.B., Robinson, J.L., Lee, E.B., Kuwabara, S., Shibuya, K., Irwin, D.J., Fang, L., Van Deerlin, V.M., Elman, L., McCluskey, L., Ludolph, A.C., Lee, V.M.Y., Braak, H., Trojanowski, J.Q., 2014. TDP-43 pathology and neuronal loss in amyotrophic lateral sclerosis spinal cord. *Acta Neuropathol.* 128, 423–437.
- Brown, R.H., Al-Chalabi, A., 2017. Amyotrophic lateral sclerosis. *N. Engl. J. Med.* 377, 162–172.
- Brunet, A., Stuart-Lopez, G., Burg, T., Scekic-Zahirovic, J., Rouaux, C., 2020. Cortical circuit dysfunction as a potential driver of amyotrophic lateral sclerosis. *Front. Neurosci.* 14.
- Burg, T., Bichara, C., Scekic-Zahirovic, J., Fischer, M., Stuart-Lopez, G., Brunet, A., Lefebvre, F., Cordero-Erausquin, M., Rouaux, C., 2020. Absence of subcortical projection neurons is beneficial in a mouse model of amyotrophic lateral sclerosis. *Ann. Neurol.* 2014, 1–30.
- Caleo, M., 2015. Rehabilitation and plasticity following stroke: insights from rodent models. *Neuroscience* 311, 180–194.
- Charcot, J.M., 1874. *Sclérose Latérale Amyotrophique : Oeuvres Complètes* Paris. Bureaux du Progrès Medical.
- Chia, R., Chiò, A., Traynor, B.J., 2017. Novel genes associated with amyotrophic lateral sclerosis: diagnostic and clinical implications. *Lancet Neurol.* 17, 94–102.
- Dentel, C., Palamituc, L., Henriques, A., Lannes, B., Spreux-Varoquaux, O., Gutknecht, L., Rene, F., Echaniz-Laguna, A., Gonzalez de Aguilar, J.-L.-L., Lesch, K.P., Meininger, V., Loeffler, J.-P.-P., Dupuis, L., 2013. Degeneration of serotonergic neurons in amyotrophic lateral sclerosis: a link to spasticity. *Brain* 136, 483–493. Available at: <https://academic.oup.com/brain/article-lookup/doi/10.1093/brain/awt274>.
- Ebstein, S.Y., Yagudayeva, I., Shneider, N.A., 2019. Mutant TDP-43 causes early-stage dose-dependent motor neuron degeneration in a TARDBP knockin mouse model of ALS. *CellReports* 26, 364–373 e4.
- Eisen, A., Braak, H., Del Tredici, K., Lemon, R., Ludolph, A.C., Kiernan, M.C., 2017. Cortical influences drive amyotrophic lateral sclerosis. *J. Neurol. Neurosurg. Psychiatry* 88, 917–924.
- Fame, R.M., MacDonald, J.L., Macklis, J.D., 2011. Development, specification, and diversity of callosal projection neurons. *Trends Neurosci.* 34, 41–50.
- Farrarwell, N.E., Lambert-Smith, I.A., Warraich, S.T., Blair, I.P., Saunders, D.N., Hatters, D.M., Yerbury, J.J., 2015. Distinct partitioning of ALS-associated TDP-43, FUS and SOD1 mutants into cellular inclusions. *Sci. Rep.* 1–14.
- Fil, D., DeLoach, A., Yadav, S., Alkam, D., MacNicol, M., Singh, A., Compadre, C.M., Gsellner, J.J., O'Brien, C.A., Fahmi, T., Basnakian, A.G., Calingasan, N.Y., Klessner, J.L., Flint Beal, M., Peters, O.M., Metterville, J., Brown Jr., R.H., Ling, K.K. Y., Rigo, F., Özdinler, P.H., et al., 2016. Mutant Profilin1 transgenic mice recapitulate cardinal features of motor neuron disease. *Hum. Mol. Genet.* 364, ddw429.
- Geevasinga, N., Menon, P., Özdinler, P.H., Kiernan, M.C., Vucic, S., 2016. Pathophysiological and diagnostic implications of cortical dysfunction in ALS. *Nat. Rev. Neurol.* 1–11. Available at: <https://www-nature-com.proxy.insermbiblio.inist.fr/articles/nrneurol.2016.140>.
- Gunes, Z.I., Kan, V.W.Y., Ye, X.Q., Liebscher, S., 2020. Exciting complexity: the role of motor circuit elements in ALS pathophysiology. *Front. Neurosci.* 14, 1–30.
- Guo, W., Fumagalli, L., Prior, R., Van Den Bosch, L., 2017. Current advances and limitations in modeling ALS/FTD in a dish using induced pluripotent stem cells. *Front. Neurosci.* 11, 1282.
- Hardiman, O., Al-Chalabi, A., Chiò, A., Corr, E.M., Logroscino, G., Robberecht, W., Shaw, P.J., Simmons, Z., van den Berg, L.H., 2017. Amyotrophic lateral sclerosis. *Nat. Rev.* 3, 17071.
- Herdewyn, S., Cirillo, C., Van Den Bosch, L., Robberecht, W., Berghe, P.V., Van Damme, P., 2014. Prevention of intestinal obstruction reveals progressive neurodegeneration in mutant TDP-43(A315T) mice. *Mol. Neurodegener.* 9, 1–14.
- Ilieva, H., Polymenidou, M., Cleveland, D.W., 2009. Non-cell autonomous toxicity in neurodegenerative disorders: ALS and beyond. *J. Cell Biol.* 187, 761–772.
- Ivanhoe, C.B., Reistetter, T.A., 2004. Spasticity. *Am. J. Phys. Med. Rehabil.* 83, S3–S9.
- Kassubek, J., Muller, H.P., Del Tredici, K., Brettschneider, J., Pinkhardt, E.H., Lule, D., Bohm, S., Braak, H., Ludolph, A.C., 2014. Diffusion tensor imaging analysis of sequential spreading of disease in amyotrophic lateral sclerosis confirms patterns of TDP-43 pathology. *Brain* 137, 1733–1740. Available at: <https://academic.oup.com/brain/article-lookup/doi/10.1093/brain/awu090>.
- Khademullah, C.S., Agrabawi, A.J., Place, K.M., Dargaei, Z., Liang, X., Pressey, J.C., Bedard, S., Yang, J.W., Garand, D., Keramidis, I., Gasecka, A., Côté, D., De Koninck, Y., Keith, J., Zinman, L., Robertson, J., Kim, J.C., Woodin, M.A., 2020. Cortical interneuron-mediated inhibition delays the onset of amyotrophic lateral sclerosis. *Brain* 143, 800–810.
- Lee, J., Hyeon, S.J., Im, H., Ryu, H., Kim, Y., Ryu, H., 2016. Astrocytes and microglia as non-cell autonomous players in the pathogenesis of ALS. *Exp. Neurobiol.* 25, 233.
- Lemon, R.N., 2008. Descending pathways in motor control. *Annu. Rev. Neurosci.* 31, 195–218.
- Liu, Y., Pattamatta, A., Zu, T., Reid, T., Bardhi, O., Borchelt, D.R., Yachnis, A.T., Ranum, L.P.W., 2016. C9orf72 BAC mouse model with motor deficits and neurodegenerative features of ALS/FTD. *Neuron* 90, 521–534.
- Lodato, S., Rouaux, C., Quast, K.B., Jantrachotechachawan, C., Studer, M., Hensch, T.K., Arlotta, P., 2011. Excitatory projection neuron subtypes control the distribution of local inhibitory interneurons in the cerebral cortex. *Neuron* 69, 763–779.
- Lodato, S., Shetty, A.S., Arlotta, P., 2014. Cerebral cortex assembly: generating and reprogramming projection neuron diversity. *Trends Neurosci.* 38, 117–125. Available at: <https://linkinghub.elsevier.com/retrieve/pii/S0166223614002112>.
- Loy, K., Bareyre, F., 2019. Rehabilitation following spinal cord injury: how animal models can help our understanding of exercise-induced neuroplasticity. *Neural Regen. Res.* 14, 405.
- Lutz, C., 2018. Mouse models of ALS: past, present and future. *Brain Res.* 1693, 1–10.
- Mackenzie, I.R.A., Bigio, E.H., Ince, P.G., Geser, F., Neumann, M., Cairns, N.J., Kwong, L.K., Forman, M.S., Ravits, J., Stewart, H., Eisen, A., McCluskey, L., Kretschmar, H.A., Monoranu, C.M., Highley, J.R., Kirby, J., Siddique, T., Shaw, P.J., Lee, V.M.Y., Trojanowski, J.Q., 2007. Pathological TDP-43 distinguishes sporadic amyotrophic lateral sclerosis from amyotrophic lateral sclerosis with SOD1 mutations. *Ann. Neurol.* 61, 427–434.
- Madisen, L., Zwingman, T.A., Sunkin, S.M., Oh, S.W., Zariwala, H.A., Gu, H., Ng, L.L., Palmiter, R.D., Hawrylycz, M.J., Jones, A.R., Lein, E.S., Zeng, H., 2009. A robust and high-throughput Cre reporting and characterization system for the whole mouse brain. *Nat. Neurosci.* 13, 133–140.
- Maier, M., Welt, T., Wirth, F., Montrasio, F., Preisig, D., McAfoose, J., Vieira, F.G., Späni, C., Stehle, T., Perrin, S., Weber, M., Hock, C., Nitsch, R.M., Grimm, J., 2018. A human-derived antibody targets misfolded SOD1 and ameliorates motor symptoms in mouse models of amyotrophic lateral sclerosis. *Sci. Transl. Med.* 10, 1–14.
- Marques, C., Fischer, M., Keime, C., Burg, T., Brunet, A., Scekic-Zahirovic, J., Rouaux, C., 2019. Early alterations of RNA metabolism and splicing from adult corticospinal neurons in an ALS mouse model. *bioRxiv*. <https://doi.org/10.1101/667733>.
- Matho, et al., 2020. Genetic dissection of glutamatergic neuron subpopulations and developmental trajectories in the cerebral cortex. *bioRxiv*. <https://doi.org/10.1101/2020.04.22.054064>.
- McAlary, L., Plotkin, S.S., Yerbury, J.J., Cashman, N.R., 2019. Prion-like propagation of protein misfolding and aggregation in amyotrophic lateral sclerosis. *Front. Mol. Neurosci.* 12, 799.
- Menon, P., Kiernan, M.C., Vucic, S., 2015. Clinical neurophysiology. *Clin. Neurophysiol.* 126, 803–809.
- Molyneaux, B.J., Arlotta, P., Menezes, J.R.L., Macklis, J.D., 2007. Neuronal subtype specification in the cerebral cortex. *Nat. Rev. Neurosci.* 8, 427–437.
- Munoz, D.G., Neumann, M., Kusaka, H., Yokota, O., Ishihara, K., Terada, S., Kuroda, S., Mackenzie, I.R., 2009. FUS pathology in basophilic inclusion body disease. *Acta Neuropathol.* 118, 617–627.
- Neumann, M., Sampathu, D.M., Kwong, L.K., Truax, A.C., Micsenyi, M.C., Chou, T.T., Bruce, J., Schuck, T., Grossman, M., Clark, C.M., McCluskey, L.F., Miller, B.L., Masliah, E., Mackenzie, I.R., Feldman, H., Feiden, W., Kretschmar, H.A., Trojanowski, J.Q., Lee, V.M.Y., 2006. Ubiquitinated TDP-43 in frontotemporal lobar degeneration and amyotrophic lateral sclerosis. *Science* 314, 130–133.
- Nihei, K., Kowall, N.W., 1993. Involvement of NPY-immunoreactive neurons in the cerebral cortex of amyotrophic lateral sclerosis patients. *Neurosci. Lett.* 1–4.
- Nolan, M., Scott, C., Gamarrallage, M.P., Lunni, D., Carpenter, K., McDonough, E., Meyer, D., Kaanumalle, S., Santamaria-Pang, A., Turner, M.R., Talbot, K., Ansorge, O., 2020. Quantitative Patterns of Motor Cortex Proteinopathy Across ALS Genotypes, pp. 1–20.
- El Oussini, H., Scekic-Zahirovic, J., Vercruysse, P., Marques, C., Dirrig-Grosch, S., Dieterlé, S., Picchiarrelli, G., Sinniger, J., Rouaux, C., Dupuis, L., 2017. Degeneration of serotonin neurons triggers spasticity in amyotrophic lateral sclerosis. *Ann. Neurol.* 82, 444–456.

- Ozdinler, P.H., Benn, S., Yamamoto, T.H., Guzel, M., Brown, R.H., Macklis, J.D., 2011. Corticospinal motor neurons and related subcerebral projection neurons undergo early and specific neurodegeneration in hSOD1G93A transgenic ALS mice. *J. Neurosci.* 31, 4166–4177.
- Prasad, A., Bharathi, V., Sivalingam, V., Girdhar, A., Patel, B.K., 2019. Molecular mechanisms of TDP-43 misfolding and pathology in amyotrophic lateral sclerosis. *Front. Mol. Neurosci.* 12, 1199.
- Purves, D., Augustine, G.J., Fitzpatrick, D., Hall, W.C., LaMantia, A.-S.-S., McNamara, J. O., Williams, S.M., 2004. Neuroscience Sinauer Associates, Inc.
- Ragagnin, A.M.G., Shadfar, S., Vidal, M., Jamali, M.S., Atkin, J.D., 2019. Motor neuron susceptibility in ALS/FTD. *Front. Neurosci.* 13, 1–37.
- Rouaux, C., Panteleeva, I., Rene, F., Gonzalez de Aguilar, J.-L.-L., Echaniz-Laguna, A., Dupuis, L., Menger, Y., Boutillier, A.-L.-L., Loeffler, J.-P.-P., 2007. Sodium valproate exerts neuroprotective effects in vivo through CREB-binding protein-dependent mechanisms but does not improve survival in an amyotrophic lateral sclerosis mouse model. *J. Neurosci.* 27, 5535–5545.
- Scekic-Zahirovic, J., El Oussini, H., Mersmann, S., Drenner, K., Wagner, M., Sun, Y., Allmeroth, K., Dieterlé, S., Sinniger, J., Dirrig-Grosch, S., Rene, F., Dormann, D., Haass, C., Ludolph, A.C., Lagier-Tourenne, C., Storkebaum, E., Dupuis, L., 2017. Motor neuron intrinsic and extrinsic mechanisms contribute to the pathogenesis of FUS-associated amyotrophic lateral sclerosis. *Acta Neuropathol.* 133, 887–906.
- Scekic-Zahirovic, J., Fischer, M., Lopez, G.S., Burg, T., Birling, M.-C.-C., Kessler, P., Rouaux, C., 2020. Genetic ablation of SOD1^{G37R} selectively from corticofugal projection neurons protects corticospinal neurons from degeneration without affecting ALS onset and progression. *bioRxiv*. <https://doi.org/10.1101/2020.01.09.900944>.
- Serio, A., Patani, R., 2017. Concise review: the cellular conspiracy of amyotrophic lateral sclerosis. *Stem Cells* 36, 293–303.
- Shibuya, K., Park, S.B., Geevasinga, N., Menon, P., Howells, J., Simon, N.G., Huynh, W., Noto, Y.-I.-I., Götz, J., Kril, J.J., Ittner, L.M., Hodges, J., Halliday, G., Vucic, S., Kiernan, M.C., 2016. Motor cortical function determines prognosis in sporadic ALS. *Neurology* 87, 513–520.
- Sorenson, E.J., 2012. The electrophysiology of the motor neuron diseases. *Neurol. Clin.* 30, 605–620.
- Strong, M.J., Gordon, P.H., 2005. Primary lateral sclerosis, hereditary spastic paraplegia and amyotrophic lateral sclerosis: discrete entities or spectrum? *Amyotroph. Lateral Scler.* 6, 8–16.
- Thomsen, G.M., Gowing, G., Latter, J., Chen, M., Vit, J.P., Staggenborg, K., Avalos, P., Alkaslasi, M., Ferraiuolo, L., Likhite, S., Kaspar, B.K., Svendsen, C.N., 2014. Delayed disease onset and extended survival in the SOD1G93A rat model of amyotrophic lateral sclerosis after suppression of mutant SOD1 in the motor cortex. *J. Neurosci.* 34, 15587–15600.
- Tremblay, R., Lee, S., Rudy, B., 2016. GABAergic interneurons in the neocortex: from cellular properties to circuits. *Neuron* 91, 260–292.
- van Es, M.A., Hardiman, O., Chiò, A., Al-Chalabi, A., Pasterkamp, R.J., Veldink, J.H., van den Berg, L.H., 2017. Amyotrophic lateral sclerosis. *Lancet* 390, 2084–2098.
- Vergouts, M., Marinangeli, C., Ingelbrecht, C., Genard, G., Schakman, O., Sternotte, A., Calas, A.-G.-G., Hermans, E., 2015. Early ALS-type gait abnormalities in AMP-dependent protein kinase-deficient mice suggest a role for this metabolic sensor in early stages of the disease. *Metab. Brain Dis.* 30, 1369–1377.
- Verstraete, E., Veldink, J.H., van den Berg, L.H., van den Heuvel, M.P., 2013. Structural brain network imaging shows expanding disconnection of the motor system in amyotrophic lateral sclerosis. *Hum. Brain Mapp.* 35, 1351–1361.
- Vucic, S., Kiernan, M.C., 2006. Novel threshold tracking techniques suggest that cortical hyperexcitability is an early feature of motor neuron disease. *Brain* 129, 2436–2446.
- Vucic, S., Kiernan, M.C., 2017. Transcranial magnetic stimulation for the assessment of neurodegenerative disease. *Neurotherapeutics* 14, 91–106.
- Vucic, S., Nicholson, G.A., Kiernan, M.C., 2008. Cortical hyperexcitability may precede the onset of familial amyotrophic lateral sclerosis. *Brain* 131, 1540–1550.
- Wegorzewska, I., Bell, S., Cairns, N.J., Miller, T.M., Baloh, R.H., 2009. TDP-43 mutant transgenic mice develop features of ALS and frontotemporal lobar degeneration. *PNAS* 106, 18809–18814.
- Welnarz, Q., Dusart, I., Roze, E., 2016. The corticospinal tract: evolution, development, and human disorders. *Dev. Neurobiol.* 77, 810–829.
- Weskamp, K., Tank, E.M., Miguez, R., McBride, J.P., Gómez, N.B., White, M., Lin, Z., Moreno Gonzalez, C., Serio, A., Sreedharan, J., Barmada, S.J., 2019. Shortened TDP43 isoforms upregulated by neuronal hyperactivity drive TDP43 pathology in ALS. *J. Clin. Invest.*
- Yasvoina, M.V., Genc, B., Jara, J.H., Sheets, P.L., Quinlan, K.A., Milosevic, A., Shepherd, G.M.G., Heckman, C.J., Ozdinler, P.H., 2013. eGFP expression under UCHL1 promoter genetically labels corticospinal motor neurons and a subpopulation of degeneration-resistant spinal motor neurons in an ALS mouse model. *J. Neurosci.* 33, 7890–7904.
- Zang, D.W., Cheema, S.S., 2002. Degeneration of corticospinal and bulbospinal systems in the superoxide dismutase 1. *Neurosci. Lett.* 332, 99–102.
- Zhang, W., et al., 2016. Hyperactive somatostatin interneurons contribute to excitotoxicity in neurodegenerative disorders. *Nat. Neurosci.* 19, 557–559.